

Observations of Wave Energy Dissipation by Bottom Friction on Rocky Shores

OLAVO B. MARQUES^{1, a, b}, FALK FEDDERSEN^{1, a}, JAMES MACMAHAN^{2, b}, CÉSAR A. ACEVEDO-RAMIREZ^{3, c},
AND SUTARA H. SUANDA^{3, c}

^a Scripps Institution of Oceanography, University of California, San Diego, La Jolla, California

^b Oceanography Department, Naval Postgraduate School, Monterey, California

^c Department of Physics and Physical Oceanography, University of North Carolina Wilmington, Wilmington, North Carolina

(Manuscript received 28 August 2024, in final form 12 December 2024, accepted 5 February 2025)

ABSTRACT: Nearshore wave dissipation by bottom friction can significantly attenuate surface waves when seabed roughness is large. Wave dissipation is parameterized with a friction factor f_e , depending upon the wave orbital excursion at the seabed A_b , and the seabed roughness k_N . Parameterizations have been developed assuming small roughness k_N relative to A_b , but whether they yield accurate f_e for rough seabeds, such as rocky shores, is unclear. Observations from a month-long experiment measured wave transformation on a rough rocky shore, with a large standard deviation of bottom depth σ_h of 0.5–1.5 m. The explicit f_e dependence on variable rocky seabed σ_h has yet to be demonstrated. Sea-swell energy flux consistently decays shoreward of 8-m water depth, which is well offshore of the surfzone given the time-mean incident significant wave height of 1 m. The observed cross-shore flux convergence yields f_e estimates across the instrument array. Quality control criteria are implemented to reduce noise in estimated f_e . Hourly f_e vary from 1 to 10 and increase with smaller A_b/σ_h , and binned means indicate a power-law scaling. When using a spatially averaged standard deviation σ_h^{eff} , the scatter around binned means increases, demonstrating that f_e is related to σ_h . Intercomparison with previous experiments is challenging due to different methodologies and definitions of f_e . Nevertheless, observations from multiple experiments are broadly consistent with a power law in terms of A_b/σ_h . Given high-resolution bathymetry, our empirical f_e scaling can be used to parameterize wave dissipation over rough seabeds of coral reefs and rocky shores.

SIGNIFICANCE STATEMENT: In contrast with sandy beaches, the large seabed roughness of coral reefs and rocky shores can induce significantly larger wave dissipation by bottom friction. We present observations over a rough rocky shore, where incoming sea-swell waves are largely dissipated by bottom friction offshore of the surfzone. While theoretical expressions can estimate the wave friction factor f_e for small seabed roughness, our results provide an empirical power law for f_e , which can be used to parameterize dissipation in wave transformation models over rough seabeds.

KEYWORDS: Wind waves; Energy budget/balance; Friction; Parameterization

1. Introduction

Surface gravity waves are important drivers of nearshore processes. For example, surface gravity waves are responsible for inducing alongshore (e.g., Feddersen et al. 1998) and rip currents (e.g., Dalrymple et al. 2011), mixing and transporting material in and out of the surf zone (e.g., Moulton et al. 2023), driving sediment transport (e.g., Sherwood et al. 2022), facilitating nutrient uptake to coral reefs (Falter et al. 2004), and impacting the settlement of benthic organisms on rocky shores (Denny 1995). The impact of sea-swell waves (5–20-s wave periods) on these processes depends on nearshore wave transformation. An important wave transformation process is the wave energy dissipation induced by bottom friction D_f , which depends both on wave conditions and the roughness of the seabed (e.g., Jonsson 1966; Nielsen 1992). For waves propagating over a sandy seabed with small bed roughness, D_f is relatively weak (e.g., Thornton and Guza 1983). In contrast, enhanced wave dissipation due to the friction associated with large bed roughness has been observed on coral reefs (e.g., Lowe et al. 2005, hereafter L05) and rocky shores (e.g., Gon et al. 2020, hereafter G20). Therefore, accurate wave dissipation

parameterizations are required to predict wave transformation over coral reefs and rocky shores.

Vertically integrated sea-swell wave dissipation D_f can be parameterized as $D_f = 0.8\rho f_e U_{\text{rms}}^3$, where ρ is the seawater density, U_{rms} is the root-mean-squared sea-swell wave velocity near the seabed, and f_e is the nondimensional wave energy dissipation factor (e.g., Jonsson 1966; Monismith et al. 2015, appendix B). The parameter f_e encodes the work done by shear and drag forces (Lowe et al. 2007). Note f_e is closely related to the wave friction factor f_w parameterizing the bottom stress in a wave boundary layer (e.g., Nielsen 1992). As $f_e \approx f_w$ is commonly assumed (Nielsen 1992), we will use the more common terminology of wave friction factor when referring to f_e . For a rough turbulent wave boundary layer, f_e depends on A_b/k_N , the ratio of the horizontal wave orbital excursion at the seabed A_b and the bed roughness parameter k_N (Nielsen 1992). Note that for both steady and oscillatory flows, k_N is not a physical distance but is a hydraulic length scale that must be determined for each specific roughness configuration (Chung et al. 2021). In a small bed roughness regime defined as $A_b/k_N \gg 1$ (i.e., the orbital wave excursions are much larger than the bed roughness), a shear-driven turbulent boundary layer is well defined, and k_N can be estimated by fitting observations to a logarithmic velocity profiles (e.g., Sleath 1987).

Corresponding author: Olavo B. Marques, omarques@ucsd.edu

DOI: 10.1175/JPO-D-24-0144.1

© 2025 American Meteorological Society. This published article is licensed under the terms of the default AMS reuse license. For information regarding reuse of this content and general copyright information, consult the AMS Copyright Policy (www.ametsoc.org/PUBSReuseLicenses).

Friction factor parameterizations that assume small roughness (i.e., $A_b/k_N \gg 1$) have f_e decreasing monotonically with A_b/k_N (e.g., Jonsson 1966; Jonsson and Carlsen 1976, hereafter JC76; Grant and Madsen 1979; Madsen 1994). These f_e parameterizations have been tested in laboratory experiments of waves propagating over immobile sand grains, gravel, and rigid roughness elements on a flat bottom (e.g., Kamphuis 1975; Sleath 1987; Simons et al. 1988; Mirfenderesk and Young 2003). For immobile sand grains, k_N is proportional to the sand grain diameter, and thus $k_N \sim O(0.1\text{--}1)$ mm (e.g., Kamphuis 1974). For mobile sediment with sand ripples or bedforms with heights $O(1)$ cm, D_f can be substantially enhanced by the turbulence generated over these bedforms (Smyth and Hay 2003), implying a k_N on the scale of the ripple (e.g., Nielsen 1992). In direct numerical simulations (DNSs) of immobile sand ripples (2-cm height and 10-cm wavelength), form drag becomes more important than the viscous forces (Barr et al. 2004). Because k_N is a hydrodynamic length scale related to a shear-driven boundary layer, no methodology exists to generally determine k_N from the physical seabed geometry alone (Chung et al. 2021). For steady flows, much effort has gone into relating the roughness geometry to k_N (Flack and Schultz 2010; Rogers et al. 2018).

Wave dissipation due to bottom friction D_f is much more important on coral reefs and rocky seabeds than on sandy seabeds, due to the significantly elevated bed roughness (e.g., Monismith 2007; G20; Davis et al. 2021). Several experiments have measured significant bottom-friction-induced sea-swell wave attenuation across fore reefs in 6–15-m water depth (Hardy and Young 1996; Péquignot et al. 2011; Monismith et al. 2015; Rogers et al. 2016, hereafter R16), reef flats with depths < 3 m (Gerritsen 1980; Nelson 1996; Falter et al. 2004; L05; Huang et al. 2012; Lentz et al. 2016, hereafter L16; Sous et al. 2023, hereafter S23), and across fore reefs with spur-and-groove formations in 5–10-m water depth (Péquignot et al. 2011; Acevedo-Ramirez et al. 2021). The vertical scale of coral reef bed roughness can be large from a few centimeters to a meter, leading to large f_e between 0.1 and 5, which are much larger than f_e on a sandy seabed.

In addition to coral reefs, rocky shores have recently been recognized as sites with potentially large bottom-friction-induced wave dissipation and can be categorized as platforms and rough rocky seabeds. Platforms can be smooth or rough, with a standard deviation of seabed elevation ranging from $O(1\text{--}20)$ cm, leading to f_e between 0.001 and 0.7 (Poate et al. 2018). On rough rocky shores, large and steep rock formations of up to several meters high can be distributed along the shoreline, in the nearshore, and throughout the continental shelf (MacMahan et al. 2024). On a rough [$O(1)$ -m variability] rocky seabed, sea-swell wave attenuation between 8- and 6-m water depth was strong with estimated f_e between 4 and 34 (G20).

Bed roughness k_N has been estimated on coral reefs (e.g., R16) by fitting the known f_e and A_b to an existing large A_b/k_N parameterization (e.g., Madsen 1994, hereafter M94). The estimated bed roughness (k_N between 0.06 and 2.5 m) leads to smaller A_b/k_N (between 0.1 and 10) than on sandy seabeds. In large roughness (i.e., $A_b/k_N \leq 1$) regimes, the underlying assumptions of a traditional shear-driven turbulent wave

boundary layer over a flatbed break down (Chung et al. 2021). Instead, flow around canopy elements increases the energy loss due to work done by drag forces (e.g., Lowe et al. 2007; Rosman and Hench 2011; Monismith et al. 2015; Yu et al. 2018). As k_N is a hydrodynamic property that cannot be elucidated directly from observations of the rough seabed (e.g., Chung et al. 2021), how the seabed variability or geometry should be implemented in D_f parameterizations for small A_b/k_N regimes is unclear. Moreover, given differences in the relevant wave dissipation processes, the appropriate f_e over rough seabeds may not follow existing large A_b/k_N parameterizations extrapolated toward $A_b/k_N \leq 1$. Therefore, new D_f parameterizations that are based solely on quantities directly known by a wave model are required to improve wave predictions over coral reefs and rocky shores.

The standard deviation of the seabed elevation σ_h is the simplest metric of seabed variability. On coral reefs and rocky seabeds, σ_h can vary from a few centimeters (L05) to 0.9 m (G20). In extrapolating f_e parameterizations developed for $A_b/k_N \gg 1$, it has been suggested that $k_N \approx 4\sigma_h$ (L05; S23). Additional statistics of seabed elevation (e.g., skewness) may provide higher-order corrections to k_N (Dealbera et al. 2024). Observations of f_e , A_b , and σ_h (L05; L16; G20; S23) yield empirical relationships between f_e and A_b/σ_h , which are primarily based on temporally variable A_b due to the few number of locations where f_e was estimated, or limited bathymetric observations. S23 estimated f_e at three sites that had σ_h varying between 8 and 15 cm, allowing some insight into the effect of variable σ_h on f_e . Yet, the impact of variable roughness on f_e has yet to be quantified.

Here, we will estimate friction factors at many locations on a rocky seabed, and we will scale observed friction factors f_e with A_b/σ_h where variable σ_h is estimated from the bathymetry. We present observations from the first Rocky Shores: Experiment and Simulations (ROXSI) experiment from the summer of 2022, which reveal strong cross-shore sea-swell wave attenuation by bottom friction. We describe the site of the experiment, the instrument array, and the data processing in section 2. An overview of the wave conditions during the experiment indicates significant wave attenuation offshore of the surf-zone (sections 3a,b). The friction factor f_e is estimated across instrument pairs from the cross-shore energy flux, and quality control criteria are applied to reduce the impact of estimation noise on f_e (sections 3c,d). The relationship between f_e and A_b/σ_h across instrument pairs is examined, where we find that f_e is partly due to the spatial variability in σ_h (section 3e). Effects of wave direction in our estimates are discussed (section 4a), and the observed friction factors are compared with previous field measurements on coral reefs and rocky shores (sections 4b,c). We conclude with a summary of our results (section 5).

2. Experiment description, methods, and overview of observations

a. Field site

This ROXSI field experiment took place from 15 June to 21 July 2022, on the rocky shoreline of the Monterey

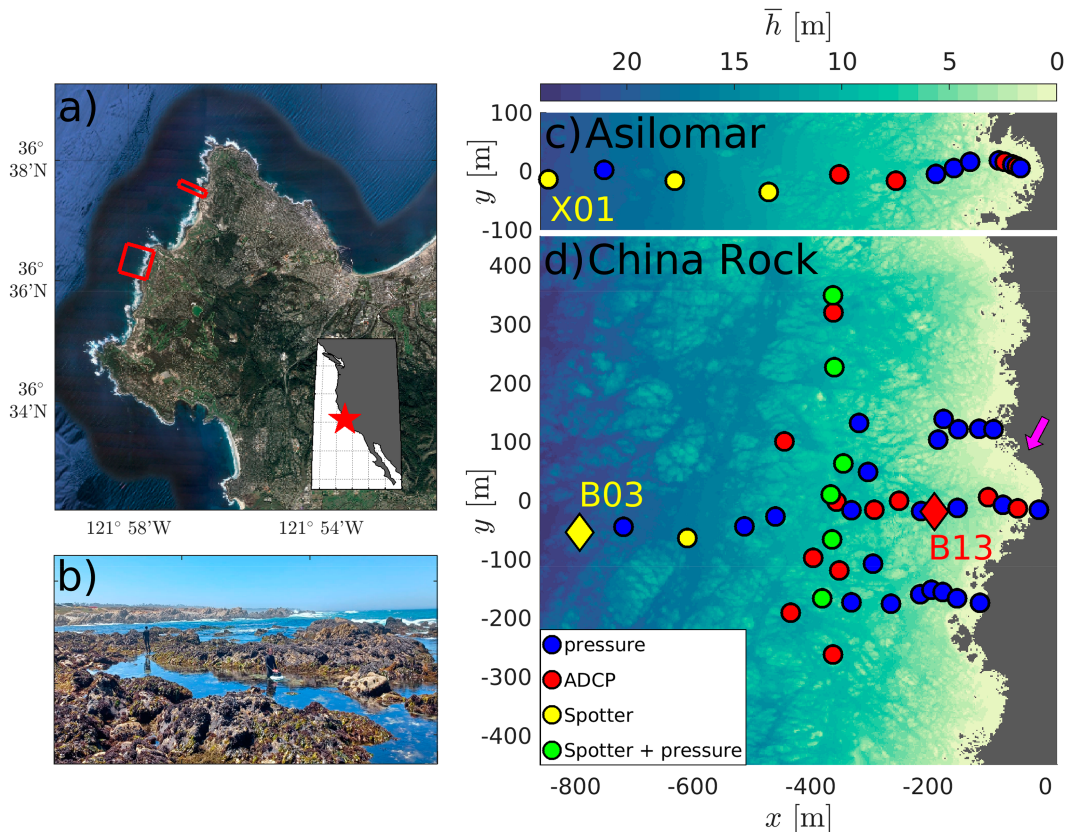


FIG. 1. Study site bathymetry and instrument array: (a) Monterey Peninsula, California, United States (the inset shows the location of the peninsula along the west coast of North America). Red rectangles in (a) show the locations of the instrument arrays at Asilomar and China Rock. (b) Photograph of the rocky shoreline at China Rock. Water depth relative to mean sea level (\bar{h}) with overlaid instrument arrays at (c) Asilomar and (d) China Rock, as functions of local cross-shore x and alongshore y coordinates. The photograph in (b) was taken from the location indicated by the magenta arrow in (d). Dots are colored by type of measurement: pressure sensors (blue), ADCPs (red), Spotter wave buoys (yellow), and Spotters with collocated pressure sensors (green). Instrument locations B03 and B13 (diamonds) are used in Figs. 3 and 4.

Peninsula, California, United States (Fig. 1). Our measurements were distributed in two regions along the peninsula separated by nearly 3 km: Asilomar State Marine Reserve (Pacific Grove) and China Rock (Pebble Beach). In each region, a local cross-shore (x) and alongshore (y) right-handed coordinate system was defined where $+x$ is directed onshore. The origin of the coordinate system at China Rock (Asilomar) is at latitude $36^{\circ}36'15.8928''\text{N}$ ($36^{\circ}37'26.5187''\text{N}$), longitude $121^{\circ}57'33.8134''\text{W}$ ($121^{\circ}56'25.1905''\text{W}$), and $+x$ is directed to 105° (113°) clockwise from the geographic north.

Rough rocky shores have topography and bathymetry variability across a wide range of scales (Figs. 1b–d). The corrugated shoreline at Asilomar and China Rock has headlands and embayments at an alongshore scale of 100 m. Rock formations, up to a few meters high, are prevalent along the coastline (Fig. 1b) and throughout the shelf where our instruments were deployed (Figs. 1c,d). The large-scale cross-shore bathymetry, i.e., across length scales much longer than the rock formations, has a relatively large slope of 1:40.

The rocky morphology changes primarily on geological time scales such that multiple datasets can be combined to

map the bathymetry. For water depths typically deeper than 10 m, historical multibeam data gridded at 2-m resolution are available from the California State University, Monterey Bay (CSUMB and Seafloor Mapping Laboratory 2014). The multibeam bathymetry has an uncertainty in the vertical elevation of $\pm 5 \text{ cm}^{-1}$ (Barnard et al. 2011). At shallower water, data come primarily from bathymetric lidar by the Joint Airborne lidar Bathymetry Technical Center of Expertise (JALBTCX). The point cloud lidar data have an irregular spatial distribution, with a typical spacing of 0.5–2 m between data points, where the individual point error is $\sim 15 \text{ cm}$ (OCM Partners 2025). The bathymetry at depths shallower than about 10 m was also mapped with an echosounder and a survey-grade GPS mounted on a Rotinor Divejet underwater scooter that is operated at the sea surface. The echosounder is a feature of the Nortek Signature1000 acoustic Doppler current profiler (ADCP) mounted at the front of the Divejet, and this system yields bottom depth data at submeter resolution along surveyed tracks. The gridded bathymetry was computed by averaging elevations relative to mean sea level z_{msl} within $2 \text{ m} \times 2 \text{ m}$ boxes in (x, y) , and we refer to the water depth as $\bar{h} = -z_{\text{msl}}$.

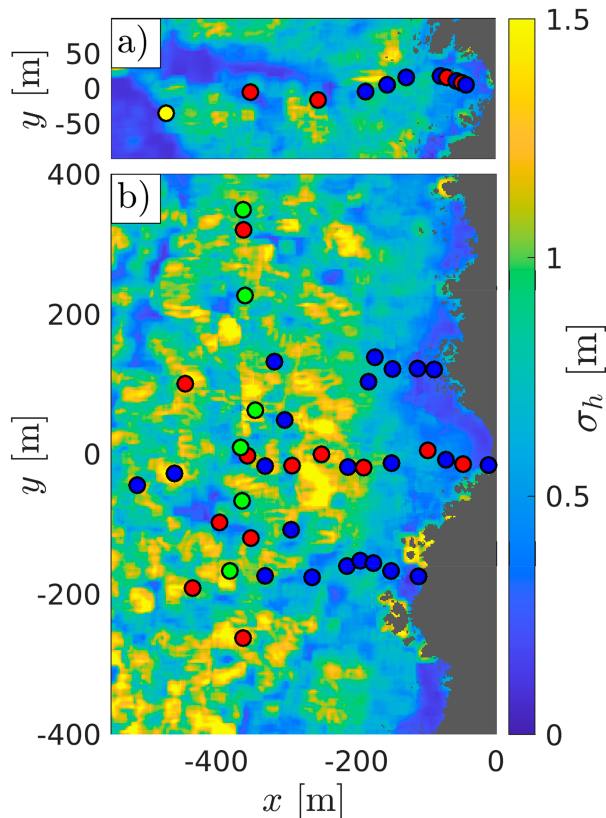


FIG. 2. Maps of the standard deviation of bottom depth σ_h as a function of local cross-shore (x) and alongshore (y) coordinate systems at (a) Asilomar and (b) China Rock. Dots denote instrument locations as in Fig. 1.

b. Bottom roughness

Throughout this paper, we characterize the seabed roughness with the standard deviation of bottom depth $\sigma_h(x, y)$ (Fig. 2). The ungridded bathymetric elevations within 20 m by 20 m boxes were used to compute σ_h at 2-m resolution. Elevations in each box were first detrended with a plane fit, and the standard deviation σ_h was computed as the root-mean-squared of detrended bottom depth within each box. Our choice for the 20-m length scale is based on a trade-off between statistical reliability of σ_h and resolving spatial variability of σ_h between our instrument sites, where the typical cross-shore spacing is between 30 and 70 m. Regions with low concentration of bathymetry data have 0.5 elevation data points per square meter, such that σ_h is computed from at least 200 data points. Given the box size, the longest horizontal length scale included in σ_h is 20 m. Given the data density, σ_h represents variability longer than 1–4 m depending on the location and data density.

As expected from the rocky morphology (Fig. 1c), large σ_h is observed at our study site (Fig. 2). The spatially averaged σ_h at China Rock and Asilomar are 0.81 and 0.62 m, respectively. In terms of the 10% and 90% quantiles, σ_h ranges from 0.42 to 1.18 m at China Rock and from 0.19 to 1.00 m at Asilomar. These statistics quantify the smaller bottom roughness

at Asilomar, which is partly due to wide sandy patches with low σ_h [e.g., at $(x, y) = (-400, 25)$ m in Fig. 2a], and partly due to smaller rocks than at China Rock. The σ_h in our study sites is larger than on coral reefs, where σ_h typically varies from 2 to 20 cm (L05; Nunes and Pawlak 2008; Amador et al. 2020; S23). The larger σ_h in our study site is consistent with results from MacMahan et al. (2024), where bathymetry data from several coral reefs and rocky shores indicate the average σ_h on the latter is 3 times larger.

c. Instrument array and data processing

We deployed instrument arrays off Asilomar, Pacific Grove within the Asilomar State Marine Reserve, and off China Rock, Pebble Beach (Figs. 1c,d), between 15 June and 21 July 2022. The instrument array at Asilomar is an approximate cross-shore transect from $\bar{h} = 21$ m to $\bar{h} = 2$ m extending off a small embayment, where instruments at shallower water ($x > -100$ m in Fig. 1c) were deployed within a deeper channel along the northern half of the embayment. The more extensive array at China Rock consists primarily of three cross-shore transects (at $y = -200$ m, $y = 0$ m, and $y = 100$ m) with additional instruments deployed in the alongshore for $6 \leq \bar{h} \leq 14$ m.

This paper focuses on sea-swell wave-resolving observations from wave buoys, ADCPs, and pressure sensors. Wave buoys were deployed at water depths of 10 m or deeper, and most ADCPs and pressure sensors were deployed in $\bar{h} \leq 10$ m. SOFAR Spotter wave buoys (Herbers et al. 2012; Raghukumar et al. 2019), which provide GPS-based vertical and horizontal sea surface displacements at a sampling rate of 2.5 Hz, were deployed for $\bar{h} \geq 10$ m. The wave buoys distributed in the alongshore around $\bar{h} \approx 10$ m at China Rock were directly cabled to bottom-mounted RBR Coda pressure sensors measuring at 2 Hz. Additional near-bottom pressure measurements were made by either RBR soloDs or internal pressure sensors from ADCPs at sampling rates between 2 and 8 Hz. We subtracted the atmospheric pressure from our pressure data based on measurements at the Monterey Harbor (≈ 6 km from our instrument arrays) by the National Oceanic and Atmospheric Administration.

Sea surface elevation spectra $S_\eta(f)$, where f is the frequency, are directly computed from vertical displacements measured by wave buoys. We computed hourly spectra using 120-s-long segments with 50% overlap and tapered with a Hanning window. The resulting frequency resolution is approximately 0.008 Hz with 118 degrees of freedom. Pressure spectra $S_p(f)$ are calculated in the same manner and are converted to $S_\eta(f)$ via

$$S_\eta = K^2 S_p, \quad (1)$$

where S_p is the spectrum calculated from pressure in units of meters (converted from Pa by normalizing with $\rho_0 g$, where $\rho_0 = 1025 \text{ kg m}^{-3}$, and gravitational acceleration $g = 9.8 \text{ m s}^{-2}$) and K is the transfer function from linear wave theory, which is as follows:

$$K = \frac{\cosh(kh)}{\cosh(kz_{\text{hab}})}, \quad (2)$$

where k is the wavenumber, h is the water depth, and z_{hab} is the height above the bottom of the pressure measurement

(e.g., Guza and Thornton 1980; Bishop and Donelan 1987). The wavenumber was estimated from the dispersion relationship of linear surface gravity waves, i.e.,

$$\omega^2 = gk \tanh(kh), \tag{3}$$

where ω is the radian wave frequency ($\omega = 2\pi f$).

The flat-bottom approximation assumed in (2) leads to errors in estimates of significant wave heights from pressure sensors (Marques et al. 2024). Collocated instruments in the China Rock array around $\bar{h} = 10$ m show that pressure sensors consistently overestimate the significant wave height from wave buoys when (2) is evaluated at the local depth measured by a pressure sensor. When evaluating (2) with a spatially averaged water depth within a radius $r = 13$ m of each pressure sensor, errors in pressure-based wave heights are reduced to $\pm 10\%$. We followed the approach outlined in Marques et al. (2024) and calculated a depth correction to the pressure sensor observations based on the mean water depth around each instrument, where the averaging r decreases toward shallower water. Alternatively, we also estimated wave statistics using the local water depth at each pressure sensor to address the sensitivity of our results. Friction factor estimates using either the local or the spatially averaged depth are typically within 20% of each other.

From sea surface elevation spectra, we computed hourly estimates of the sea-swell significant wave height as follows:

$$H_s \equiv 4 \sqrt{\int_{SS} S_\eta(f) df}, \tag{4}$$

where the subscript SS under the integral sign denotes the sea-swell (0.05–0.2 Hz) frequency band. The high-frequency cutoff prevents overestimates of H_s from S_η contaminated at higher frequencies, where noise overwhelms a small wave-induced pressure variance. Moreover, wave buoy-estimated wave energy at $f > 0.2$ Hz and $f < 0.05$ Hz was relatively small in our experiment. Additional hourly sea-swell bulk statistics include mean period T_{mean} and mean direction θ_{mean} (see definitions in appendix A).

We will estimate sea-swell energy dissipation by bottom friction and wave friction factors, which depend on the near-bed root-mean-square (rms) orbital wave velocity U_{rms} (e.g., Monismith et al. 2015):

$$U_{\text{rms}} = \sqrt{\int_{SS} \left[\frac{2\pi f}{\sinh(kh)} \right]^2 S_\eta(f) df}, \tag{5}$$

and the horizontal orbital excursion:

$$A_b = \sqrt{2 \int_{SS} \frac{1}{\sinh^2(kh)} S_\eta(f) df}. \tag{6}$$

The $\sqrt{2}$ factor relates the root-mean-squared variability of the horizontal orbital excursion to a scale A_b for the amplitude of the corresponding orbital excursion.

d. Energy balance equation

Numerical wave models typically solve the wave action conservation equation to predict the evolution of the wave

spectrum (e.g., Booij et al. 1999). In the absence of wave–current interaction, wave action conservation simplifies to the wave energy conservation equation. We consider the sea-swell frequency-band-integrated energy equation

$$\frac{\partial E}{\partial t} + \frac{\partial F_x}{\partial x} + \frac{\partial F_y}{\partial y} = -D_b - D_f, \tag{7}$$

where E is the wave energy density, F_x and F_y are the cross-shore and alongshore components of the bulk (frequency integrated) energy flux, D_b is the wave dissipation by depth-limited wave breaking, and D_f is the wave dissipation by bottom friction. Infragravity wave energy in our study site is very weak relative to sandy beaches (at most 1% of sea-swell wave energy), and thus we neglect nonlinear triad interactions that can transfer energy from the latter into the infragravity band on sandy shorelines (Herbers et al. 1994). Energy input from the wind is also neglected. S23 determined that including wave–current interaction only weakly affected the estimated friction factor. The strength of wave–current interaction is given by the nondimensional parameter U/c , where U is the depth-averaged mean current scale and c is the wave phase speed. In S23, this parameter was ≤ 0.1 . Similarly, this parameter is also < 0.1 for our observations (not shown) justifying neglecting wave–current interaction. The components of the bulk energy flux are

$$F_x = \int_{SS} \rho_0 g a_1(f) S_\eta(f) c_g(f) df, \tag{8a}$$

$$F_y = \int_{SS} \rho_0 g b_1(f) S_\eta(f) c_g(f) df, \tag{8b}$$

where $a_1(f)$ and $b_1(f)$ are the first directional moments (appendix A) and

$$c_g(f) = c_p(f) \frac{1}{2} \left[1 + \frac{2kh}{\sinh(2kh)} \right], \tag{9}$$

is the group velocity, and c_p is the phase speed $c_p = \omega/k$.

Here, we seek to estimate the bottom-friction-induced wave dissipation D_f . In principle, the left-hand side of (7) can be applied to observations from instrument arrays to measure the total wave dissipation on the right-hand side. In practice, additional assumptions are required to simplify (7) and estimate D_f from instrument arrays. The unsteady term $\partial E/\partial t$ can be readily evaluated, and this term is negligible at all locations where significant wave dissipation was observed. Moreover, directional fluxes [(8)] can only be estimated where ADCPs and Spotter wave buoys were deployed (Figs. 1c,d), which substantially decreases the number of instrument pairs for estimating wave dissipation. However, assuming negligible reflection and small angle of incidences, $a_1 \approx 1$, $b_1 \approx 0$, (8) is approximated to

$$F_x \approx F = \int_{SS} \rho_0 g S_\eta(f) c_g(f) df, \tag{10a}$$

$$F_y \approx 0. \tag{10b}$$

This approximation allows the energy flux F to be computed for all stand-alone pressure sensors, and the wave dissipation can be computed between a larger number of instrument pairs from (10a). Onshore wave propagation with small reflection is a widely used assumption assumed to measure convergences of F from pressure sensors (e.g., Monismith et al. 2015; L16; S23). If the water depth is sufficiently deep where depth-limited wave breaking can be neglected, then $D_b = 0$ and the wave dissipation can be assumed to be entirely due to bottom friction D_f (e.g., Monismith et al. 2015). Taking all these approximations into account, we rewrite (7) as

$$\frac{dF}{dx} = -D_f + \epsilon, \quad (11)$$

where ϵ represents all the neglected processes, which can be considered as noise in the estimates of D_f and friction factor f_e .

3. Results

a. Overview of sea-swallow wave conditions

Sea-swallow wave statistics observed in our 40-day experiment were characteristic of summer mild wave conditions on the Monterey Peninsula. From our offshore wave buoy at China Rock deployed at $\bar{h} = 21$ m (B03 in Fig. 1c), H_s varied from 0.3 to 2.0 m, and T_{mean} varied from 5.8 to 11.4 s (Figs. 3a,b). Larger wave heights were mostly associated with incident waves from the northwest ($\theta_{\text{mean}} < 0$ in Fig. 3c), and the experiment-averaged mean period is $T_{\text{mean}} = 7.9$ s. Longer period waves from the southwest ($\theta_{\text{mean}} > 0$) tended to have smaller wave heights. Incident θ_{mean} at B03 rarely exceeded 20° and the 20% and 80% percentiles were -11.9° and 7.4° (Fig. 3c).

A substantial decrease in H_s is observed between the offshore wave buoy and measurements taken at $\bar{h} = 5$ m (instrument site B13, Fig. 3a). The reduction in H_s is about 0.1–0.3 m (15%–25%) and occurs in water depths greater than where depth-limited wave breaking is expected. For a saturated surfzone with $\gamma = H_s/h = \sqrt{2} \times 0.45 \approx 0.6$ (e.g., Thornton and Guza 1982), depth-limited breaking for the most energetic wave events in the experiment ($H_s \approx 2$ m) is expected to be important at water depths less than 3.5 m, which is shallower than $\bar{h} = 5$ m at B13. Although the bathymetry is rough and the water depth does not vary monotonically in the cross-shore, the smallest water depths offshore of B13 are $\bar{h} \approx 4$ m, and depth-limited wave breaking cannot account for the observed decrease in H_s between B03 and B13. The mean period T_{mean} is nearly conserved across instrument sites, and the smaller magnitude of θ_{mean} at shallower water indicates that sea-swallow waves become more normally incident as they propagate onshore. The conserved T_{mean} and the changes in θ_{mean} qualitatively agree with the sea-swallow wave transformation expected from linear wave theory with no wave dissipation (Herbers et al. 1999), while the observed decrease in H_s does not (e.g., Dean and Dalrymple 1991).

b. Cross-shore wave attenuation

Experimental time-mean sea-swallow wave statistics across the instrument array further highlight the attenuation of

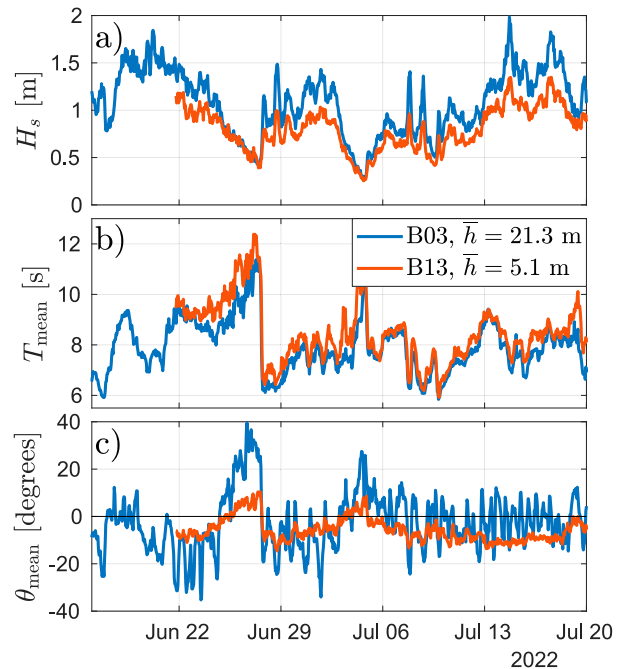


FIG. 3. Time series of (a) significant wave height H_s , (b) mean period T_{mean} , (c) mean wave direction θ_{mean} at instrument sites B03 and B13 (diamonds in Figs. 1 and 4). Sea-swallow wave statistics were computed between 0.05 and 0.2 Hz (section 2c). Time-mean water depths \bar{h} at B03 and B13 are 21 and 5 m, respectively. Positive (negative) θ_{mean} indicates waves from the southwest (northwest).

sea-swallow waves at water depths well seaward of the surfzone (Fig. 4). Most instrument locations at $\bar{h} > 8$ m have smaller time-mean H_s than observed offshore, and the average H_s decrease across these instruments is 5% (Fig. 4a). Time-mean wave height further decreases toward shallower instruments at $\bar{h} \approx 3$ m. We next examine the cross-shore evolution of the normalized wave energy flux F/F_0 (Fig. 4b) where F_0 is the most offshore wave energy flux estimated at either B03 or X01 for China Rock or Asilomar, respectively. As the wave energy flux is proportional to H_s^2 and the group velocity decreases shoreward of $\bar{h} < 15$ m (for the time-averaged mean period $T = 7.9$ s), a pronounced decrease in F/F_0 is also observed seaward of the surfzone (Fig. 4b). For $\bar{h} \leq 8$ m, the time-mean flux consistently decays toward shallower water, and F/F_0 is close to 0 at $\bar{h} = 2$ m. For $8 \leq \bar{h} \leq 13$ m, overall time-mean F/F_0 is mostly < 1 . Spatial variability in F/F_0 is potentially due to wave focusing and defocusing over the spatially variable bathymetry across the entire array. Although wave reflection at the site is weak (3%–6%, P. Collins et al. 2024), it may influence the spatial variability in F/F_0 .

The observed H_s and F/F_0 have large differences from the expected wave statistics on sandy beaches (Fig. 4). Sea-swallow wave transformation on sandy beaches is well described by a simple cross-shore model (e.g., Thornton and Guza 1983; Ruessink et al. 2001) between energy flux divergence and dissipation by wave breaking. Assuming a narrow-band wave field, Rayleigh-distributed wave heights, and a parameterization for

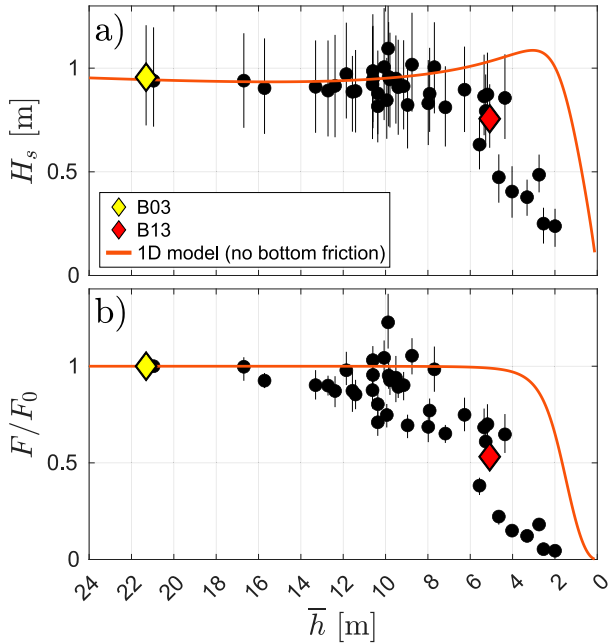


FIG. 4. Cross-shore transformation of sea-swell wave statistics as a function of mean depth \bar{h} : (a) significant wave height H_s and (b) normalized energy flux F . Energy flux is normalized by the offshore value either at B03 or X01 for China Rock or Asilomar, respectively. Symbols are experiment averages, and vertical bars show the 25% and 75% percentiles. Diamonds show observations that are also discussed in Fig. 3, and their locations are shown in Fig. 1c. The orange line is the H_s and the normalized energy flux F predicted by integrating a 1D energy balance [(11)] developed for sandy shores (Thornton and Guza 1983) using the time-mean $\bar{H}_s = 1$ m and $\bar{T}_{\text{mean}} = 7.9$ s.

wave breaking in a saturated surfzone, the energy equation can be integrated to yield the cross-shore profiles of significant wave height and energy flux (e.g., Thornton and Guza 1983). Dissipation by wave breaking was parameterized following Thornton and Guza (1983), with their standard wave breaking parameters $\gamma = 0.45$ and $B = 1$. To contrast our time-mean observations with what is expected for a sandy beach, we integrated the energy equation for a linearly sloping beach with a 1:40 slope, normally incident waves, and wave height and mean period that match the statistics in our offshore observations (i.e., $\bar{H}_s = 1$ m and $\bar{T} = 7.9$ s). The modeled F/F_0 is essentially constant for $\bar{h} \geq 5$ m and decreases $<10\%$ until $\bar{h} = 3$ m (Fig. 4b). The modeled wave height increases between $6 \leq \bar{h} \leq 3$ m, consistent with the nearly conserved F , before rapidly decreasing at water depths shallower than $\bar{h} = 2.5$ m due to wave breaking (Fig. 4a). In the range of 13–5-m water depth where wave breaking is not occurring, the modeled F and H_s are at the upper limit of the observations, indicating that nonbreaking processes are leading to the decay in the observed wave energy flux.

c. Estimation of the friction factor

The rough bathymetry at our study site (Fig. 2) and the large sea-swell attenuation seaward of the surfzone (Fig. 4

suggest that energy dissipation by bottom friction is a dominant term in the energy balance. Sea-swell wave dissipation by bottom friction can be parameterized (appendix B) by a friction factor f_e through

$$D_f = 0.8\rho f_e U_{\text{rms}}^3. \quad (12)$$

We test the hypothesis that dissipation is due to bottom friction by assuming the energy balance as follows:

$$\frac{dF}{dx} = -D_f. \quad (13)$$

Substituting (12) into (13) yields

$$f_e = -\frac{dF}{dx} \frac{1}{0.8\rho U_{\text{rms}}^3}. \quad (14)$$

To estimate f_e from our observations, hourly energy flux convergence $-dF/dx$ was computed with a finite difference between adjacent cross-shore instruments. The instrument arrays at China Rock and Asilomar have 33 pairs of adjacent instruments that are roughly aligned in the cross-shore. The U_{rms} used in (14) was the mean between the two instrument locations, which we denote by $\langle U_{\text{rms}} \rangle$, and then cubed $\langle U_{\text{rms}} \rangle^3$ for computing f_e (as in Monismith et al. 2015). Moreover, a bulk friction factor \tilde{f}_e were computed from the least squares fit between $\langle U_{\text{rms}} \rangle^3$ and $-dF/dx$, which is a proxy for the time-averaged friction factor and has less uncertainty than hourly estimates of f_e .

As an example of the f_e estimation, we show observations from one pair of instruments (B11–B12), where energy flux convergence was measured and it has an excellent agreement with the parameterized dissipation D_f (Fig. 5). Instrument locations B11 and B12 were separated by $\Delta x \approx 40$ m in the cross-shore, by $\Delta y \approx 18$ m in the alongshore, and the time-mean water depths \bar{h} were 9.8 and 7.2 m (Fig. 5a). A small but consistent decrease in H_s is observed between instruments (Fig. 5b), and the difference in time-mean \bar{H}_s is 13 cm (13%). The attenuated wave height leads to a decrease in F (Fig. 5c) and a time-averaged energy flux convergence $-dF/dx = 38 \text{ W m}^{-2}$ (Fig. 5d). The energy flux convergence is highly correlated with $\langle U_{\text{rms}} \rangle^3$, which yields squared correlation $r^2 = 0.91$ and supports that dissipation is well represented by bottom friction and the assumptions within (12) and (13). The resulting f_e vary between 2 and 12 throughout the experiment, which tends to decrease with increasing H_s , and the bulk friction factor is $\tilde{f}_e = 3.7$.

d. Quality control of instrument pairs

The observations from the ROXSI experiment provide an unprecedented number of instrument locations to estimate f_e in a single study site. However, unlike the results from instrument pair B11–B12, D_f may be small at other locations, and the energy flux balance may not be well represented by (12) and (13). To ensure reliable friction factor estimates, we applied quality control criteria to the analysis of the observations. The first category of quality control criteria applies to

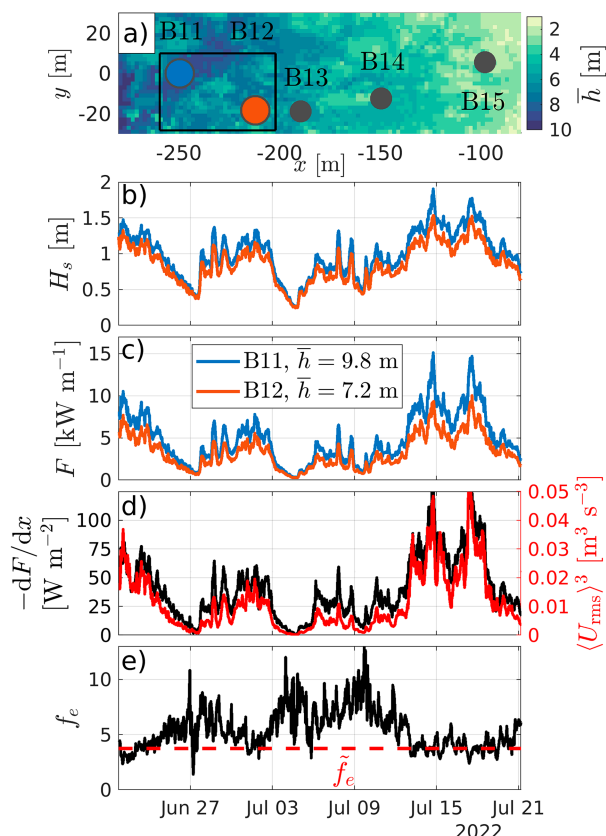


FIG. 5. Example of the estimation of f_e . (a) Bathymetry map around instrument locations B11–B15 (where the rectangle is used to compute $\langle \sigma_h \rangle$ in Fig. 6). Time series of wave statistics and friction factor estimates from B11 (blue lines) and B12 (orange lines) locations: (b) significant wave height H_s ; (c) energy flux F ; (d) energy flux convergence $-dF/dx$ (black), and the cube of the seawall root-mean-square seabed orbital velocity averaged between both sites $\langle U_{rms} \rangle^3$ (red); and (e) hourly friction factor f_e (14) and the bulk friction factor \tilde{f}_e . The correlation coefficient squared between $-dF/dx$ and $\langle U_{rms} \rangle^3$ is $r^2 = 0.91$.

the spacing of adjacent instrument pairs. The cross-shore separation (Δx) of instrument pairs is required to be in the range $20 \leq \Delta x < 120$ m. Very short instrument separation can lead to large noise in dF/dx and subsequently noisy estimates of f_e . The large Δx cutoff criterion eliminates pairs where the finite difference approximation of dF/dx and the spatial average of $\langle U_{rms} \rangle^3$ in (14) are inaccurate to estimate f_e . Second, the alignment of adjacent instruments can substantially depart from being cross-shore oriented. Thus, we require instrument pairs to have $|\Delta y/\Delta x| < \tan(30^\circ)$, where Δy is the alongshore instrument separation. These two quality control criteria remove 13 out of a total of 33 adjacent instrument pairs.

The second quality control category applies to time-dependent variables. As negative friction factor is unphysical, f_e are only estimated for positive energy flux convergence ($-dF/dx > 0$), and we removed times when $-dF/dx < 0$. Bulk \tilde{f}_e estimated without this constraint are very similar (typically within 1%) to those estimated with the constraint, indicating weak bias.

We also removed times when either an instrument in the pair has $h < 2$ m (which may occur at low tide), since the large seabed roughness for such shallow bathymetry can lead to outcropping rocks, near which wave transformation can significantly depart from the one-dimensional balance (13). Since (12)–(14) neglect wave breaking, we applied a criterion on the ratio of H_s to h to neglect observed energy flux convergence due to wave breaking. Depth-limited wave breaking approximately begins when $H_s/h > \gamma$, where γ is often taken as 0.6 (Thornton and Guza 1982), but observations on sandy beaches can vary between 0.4 and 0.8 (e.g., Sallenger and Holman 1985). We require that $H_s/h < 0.25$ as a conservative criterion to ensure that wave breaking is not contaminating the f_e estimates. Times when $H_s/h \geq 0.25$ at any instrument were removed. If either time series across an instrument pair has more than 20% of data that do not pass any quality control criterion, then the corresponding instrument pair is removed. These criteria result in the removal of five additional instrument pairs, yielding 15 instrument pairs that satisfy what we denote as the primary quality control criteria. Given both the deployment of each instrument and the quality control criteria, the average length of the time series across these 15 instrument pairs is 27.4 days, with minimum and maximum lengths of 23.25 and 34 days.

Statistics from the 15 instrument pairs that pass the primary quality control criteria are examined in Table 1, where pairs from $N = 1$ to $N = 15$ are sorted for decreasing r^2 . Our estimates of f_e span a wide range of water depths, where the mean depth between instrument sites in each pair (\bar{h}) varies from near 3 to 17 m. The cross-shore instrument spacing Δx is between 26 and 102 m, and most [(10)] instrument pairs have $|\Delta y/\Delta x| < \tan(20^\circ)$. The time-mean \bar{H}_s decreases toward shallower water across instrument pairs, on average by 0.13 m, indicating wave dissipation by bottom friction. The overall decrease in wave energy flux yields an inferred time-mean wave dissipation $-dF/dx$ ranging from 8 to 63 W m^{-2} across instrument sites, with an average of 23 W m^{-2} . The observed time-mean \bar{U}_{rms} and \bar{A}_b vary across instruments within 0.13–0.26 m s^{-1} and 0.32–0.59 m, respectively. For each instrument pair in Table 1, \bar{U}_{rms} and \bar{A}_b can increase onshore due to the effect of decreasing water depth in (5) and (6).

For the 15 locations that passed the primary quality control, we next examine the squared correlation coefficients r^2 between $-dF/dx$ and $\langle U_{rms} \rangle^3$, a metric for how well the simple wave energy balance [(13)] holds. If terms neglected in (13) are also important or if $-dF/dx$ is too noisy, then r^2 should be small. In contrast, a high r^2 supports that the underlying assumptions in (12)–(14) are valid, implying accurate hourly estimates of f_e . The squared correlation r^2 varies from 0.92 to 0.36 (Table 1) and is generally higher with larger $-dF/dx$, which suggests that (13) is a more accurate leading-order balance of the energy balance where dissipation is stronger. Overall, shallower water depths (\bar{h}) < 10 m tend to have larger $-dF/dx$ and r^2 (Table 1). For $\bar{h} \geq 10$ m, r^2 of 0.43–0.64 are among the lowest, indicating that other terms not included in (13) are nonnegligible at these depths, and that f_e estimates are less reliable. Across the 15 locations, the bulk friction factor \tilde{f}_e ranges from 1.1 to 5.1, with an average of 2.2 across the sites.

TABLE 1. Statistics of instrument pairs that passed primary quality control criteria. Cross-shore and alongshore instrument separations are denoted by Δx and Δy . The experiment averaged (denoted by an overbar) of \bar{H}_s , \bar{U}_{rms} , and \bar{A}_b is shown at each location for all instrument pairs. The mean water depth between instrument sites is denoted by $\langle \bar{h} \rangle$. The correlation coefficient squared r^2 is computed between $-dF/dx$ and $\langle U_{\text{rms}} \rangle^3$. The bulk friction factors \tilde{f}_e are given by a least squares fit between $-dF/dx$ and $\langle U_{\text{rms}} \rangle^3$. The spatially averaged standard deviation of bed elevation is given by $\langle \sigma_h \rangle$. Results are presented for decreasing r^2 .

N	ID	$\langle \bar{h} \rangle$ (m)	Δx (m)	Δy (m)	\bar{H}_s (m)	\bar{U}_{rms} (m s^{-1})	$-dF/dx$ (W m^{-2})	r^2	\tilde{f}_e	\bar{A}_b (m)	$\langle \sigma_h \rangle$ (m)
1	B11-B12	8.5	38	-18	1.00-0.86	0.19-0.21	40	0.92	3.8	0.45-0.50	1.11
2	E03-D01	9.0	102	-10	1.19-0.89	0.23-0.20	32	0.88	2.9	0.48-0.44	0.77
3	X08-X09	4.3	27	11	0.56-0.48	0.18-0.17	13	0.86	1.6	0.43-0.40	0.84
4	B14-B15	4.2	52	18	0.65-0.50	0.19-0.22	19	0.86	2.3	0.45-0.52	0.63
5	X07-X08	5.0	31	10	0.87-0.53	0.25-0.17	63	0.81	5.1	0.52-0.40	0.96
6	B12-B13	6.1	22	-1	0.87-0.81	0.21-0.25	35	0.81	2.7	0.50-0.59	1.04
7	X09-X10	3.3	49	2	0.50-0.33	0.17-0.15	13	0.80	2.1	0.40-0.37	0.69
8	X06-X07	7.2	68	12	0.96-0.84	0.19-0.24	20	0.76	1.5	0.40-0.50	0.62
9	B13-B14	5.3	40	7	0.79-0.67	0.24-0.19	17	0.71	1.4	0.59-0.46	0.86
10	A02-A04	7.0	68	-2	1.11-0.99	0.25-0.26	20	0.65	1.0	0.53-0.55	0.72
11	A01-E05	9.9	54	25	1.02-0.93	0.17-0.21	22	0.64	2.4	0.36-0.46	1.08
12	B05-B06	15.0	95	36	1.00-0.95	0.13-0.15	7	0.59	2.3	0.32-0.36	0.55
13	B09-B10	10.0	39	1	1.08-1.03	0.20-0.20	15	0.59	1.3	0.45-0.44	0.96
14	E09-D02	10.8	42	-14	0.98-0.91	0.18-0.16	13	0.43	1.8	0.43-0.36	0.99
15	B15-B16	3.0	26	-13	0.50-0.41	0.22-0.16	8	0.36	1.1	0.52-0.40	0.53

Our observed $\tilde{f}_e > 1$ are comparable to the largest estimates of the friction factor reported at very rough coral reefs (Monismith et al. 2015; R16; L16; S23) and rocky seabed (G20).

The seabed roughness for each instrument pair that passed the quality control criteria was computed as the spatially averaged standard deviation of seabed elevation $\langle \sigma_h \rangle$. The gridded σ_h was averaged within a rectangle bounding instrument locations for each pair in Table 1 (e.g., see Fig. 5a for pair $N = 1$). As an example, the large bottom depth variability around instrument pair B11-B12 is associated with σ_h between 0.8 and 1.7 m (Fig. 6). Note that variations in σ_h across horizontal scales shorter than ≈ 10 m are relatively small because σ_h was computed within $20 \text{ m} \times 20 \text{ m}$ boxes (section 2b). The bathymetry around instruments B11 and B12 yields the largest $\langle \sigma_h \rangle$ across all instrument pairs, where $\langle \sigma_h \rangle$ varies between 0.53 and 1.11 m (Table 1).

e. Dependence of f_e on A_b/σ_h

The dependence of f_e on A_b/σ_h is now addressed with the first 10 instrument pairs in Table 1 that have $r^2 \geq 0.65$. Both A_b and σ_h are averaged between instrument locations resulting in $\langle A_b \rangle$ and $\langle \sigma_h \rangle$. For these instrument pairs, the mean (time and across pairs) of $\langle A_b \rangle$ is 0.5 m. The mean of $\langle \sigma_h \rangle$ is $\sigma_h^{\text{ref}} = 0.8 \text{ m}$, with a standard deviation of 0.2 m. The observed hourly f_e are large, typically between 1 and 10, and consistently decrease with $\langle A_b \rangle / \langle \sigma_h \rangle$ that varies between 0.2 and 1 (gray dots in Fig. 7a). The correlation coefficient squared r_*^2 between the hourly $\log_{10}(f_e)$ and $\log_{10}(\langle A_b \rangle / \langle \sigma_h \rangle)$ is $r_*^2 = 0.43$ (Fig. 7a), suggesting a power-law relationship, albeit with scatter. In terms of the 25% and 75% quartiles within each $\langle A_b \rangle / \langle \sigma_h \rangle$ bin, the ratio between the upper and lower f_e quartiles is about two. In log space, the bin-averaged f_e (black dots in Fig. 7a) has a very clear linear relationship with $\langle A_b \rangle / \langle \sigma_h \rangle$, further indicating a power-law relationship.

Given the variable $\langle \sigma_h \rangle$ and the large number of instrument pairs with f_e estimates, we assess whether f_e is as effectively scaled with a uniform σ_h^{ref} by examining the f_e and $\langle A_b \rangle / \sigma_h^{\text{ref}}$ relationship (Fig. 7b). Overall, the relationship is qualitatively

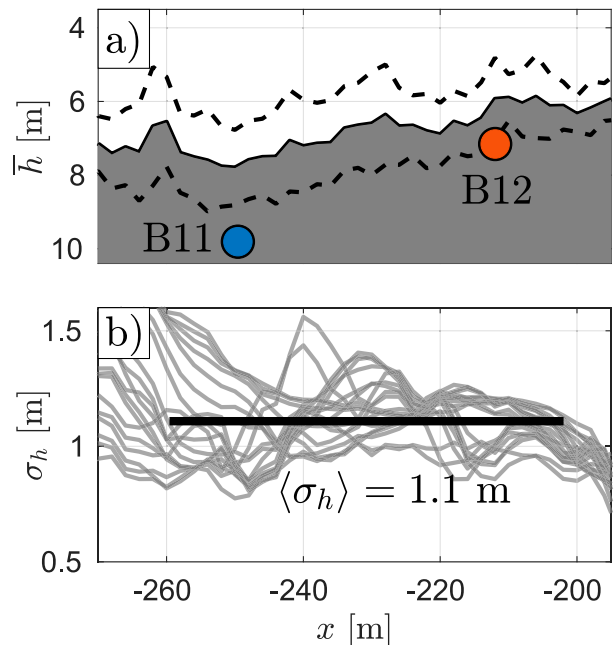


FIG. 6. (a) Alongshore-averaged \bar{h} , within the same bounds as the rectangle in Fig. 5a, where the dashed lines denote the averaged depth plus or minus one standard deviation (computed from the alongshore distribution of \bar{h}). (b) Cross-shore profiles of the standard deviation of bottom depth σ_h (gray lines), where the black line is the mean of σ_h within the rectangle in Fig. 5a. Blue and orange circles in (a) denote the locations in the cross-shore and in the vertical of instruments at locations B11 and B12.

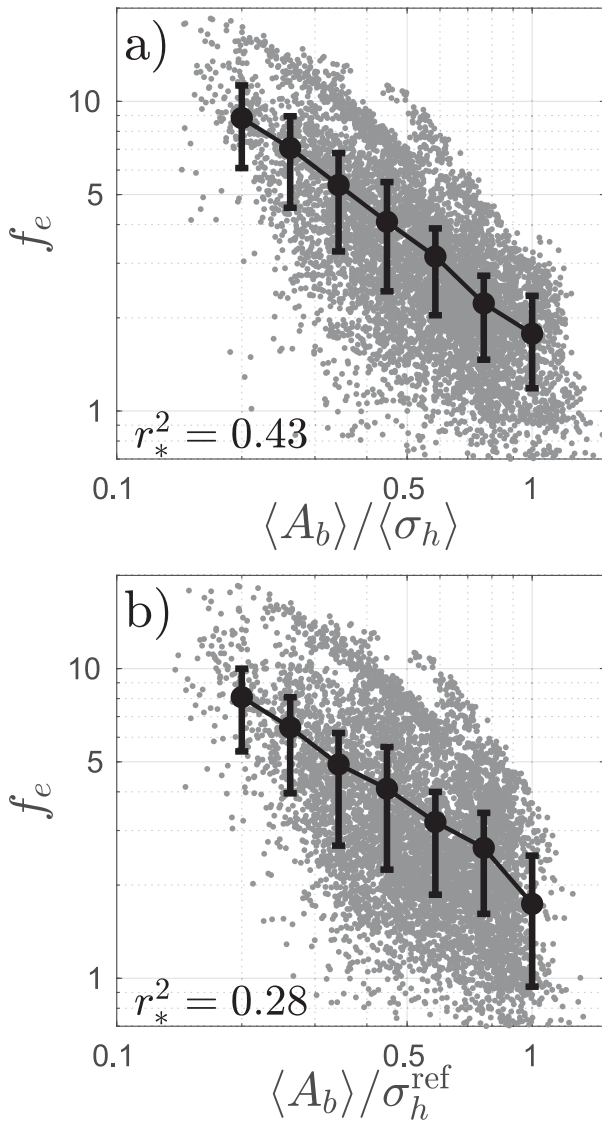


FIG. 7. Friction factor f_e vs (a) $\langle A_b \rangle / \langle \sigma_h \rangle$ and (b) $\langle A_b \rangle / \sigma_h^{\text{ref}}$, where $\langle A_b \rangle$ is the instrument-pair average orbital displacement. Two choices of the standard deviation of bed elevation are used: (a) the spatial average between instrument locations for each pair $\langle \sigma_h \rangle$, or (b) a constant average over all pairs $\sigma_h^{\text{ref}} = 0.8$ m. The gray dots are hourly estimates, the black dotted lines are binned means, and the vertical bars denote the 25%–75% quartile ranges. Only data from the 10 instrument pairs with the highest correlations ($N \leq 10$) are included. The correlation coefficient squared in (a) between $\log_{10}(f_e)$ and $\log_{10}(\langle A_b \rangle / \langle \sigma_h \rangle)$ is $r_*^2 = 0.43$ and in (b) between $\log_{10}(f_e)$ and $\log_{10}(\langle A_b \rangle / \sigma_h^{\text{ref}})$ is $r_*^2 = 0.28$.

similar to that with $\langle A_b \rangle / \langle \sigma_h \rangle$ because f_e is largely explained by temporal variability in $\langle A_b \rangle$. However, the resulting $r_*^2 = 0.28$ is substantially lower than the $r_*^2 = 0.43$ for $\langle A_b \rangle / \langle \sigma_h \rangle$. These two r_*^2 are distinct as the 95% confidence level is near ± 0.02 (Emery and Thomson 2014). The binned-mean f_e versus $\langle A_b \rangle / \sigma_h^{\text{ref}}$ reveals a less consistent power-law relationship than for $\langle A_b \rangle / \langle \sigma_h \rangle$. The 25%–75% quartile ranges for f_e versus

$\langle A_b \rangle / \sigma_h^{\text{ref}}$ are 10% larger than when using variable $\langle \sigma_h \rangle$. The improved r_*^2 , the binned-mean f_e more power-law consistent, and the smaller quartile range using $\langle A_b \rangle / \langle \sigma_h \rangle$ versus $\langle A_b \rangle / \sigma_h^{\text{ref}}$ (Fig. 7) demonstrate that variable $\langle \sigma_h \rangle$ across instrument pairs is important to setting the wave friction factor and the bottom-friction-induced wave dissipation.

The result above of larger r_*^2 when using $\langle A_b \rangle / \langle \sigma_h \rangle$ instead of $\langle A_b \rangle / \sigma_h^{\text{ref}}$ (Fig. 7) is based on 10 instrument pairs with the largest r^2 (from $N = 1$ to $N = 10$, Table 1), where f_e estimates are more reliable. We now assess the sensitivity of this result to the number N of instrument pairs used to compute r_*^2 . For $N = 2$ to $N = 15$, r_*^2 was computed using both $\langle \sigma_h \rangle$ and σ_h^{ref} with data from the first N instrument pairs that have highest r^2 (Fig. 8b). For $N \leq 10$, using variable $\langle \sigma_h \rangle$ yields $0.28 \leq r_*^2 \leq 0.43$, which is systematically larger than the $0.18 \leq r_*^2 \leq 0.28$ using σ_h^{ref} . For $N > 10$, the r_*^2 decreases for both $\langle \sigma_h \rangle$ and σ_h^{ref} . This is likely due to incorporating higher noise f_e from instrument pairs that have reduced r^2 (Fig. 8a). Nevertheless, even for $N = 14$ where the difference between results is smallest, the two r_*^2 using $\langle \sigma_h \rangle$ ($r_*^2 = 0.28 \pm 0.02$) and σ_h^{ref} ($r_*^2 = 0.21 \pm 0.02$) are distinct based on the 95% confidence limits. The consistently elevated r_*^2 using $\langle \sigma_h \rangle$ over σ_h^{ref} is a robust result and demonstrates that the spatially variable $\langle \sigma_h \rangle$ partly explains the f_e variability. Therefore, regions with larger $\langle \sigma_h \rangle$ have elevated seabed roughness that induces an increase in f_e .

4. Discussion

a. Effect of wave angle on f_e

We assumed normally incident waves in estimating the cross-shore wave energy flux (10a) and its gradient dF/dx (section 2d). Other f_e studies also require assumptions regarding wave directionality to estimate energy flux from pressure sensors. Generally, wave refraction tends to reduce the incident wave angle in the onshore direction. For studies over reef flats (L05; S23), forereef measurements indicate a small incident mean wave angle, suggesting that assuming unidirectional wave propagation is reasonable. From numerical simulations, refraction across the reef flat was estimated to induce biases in observed $-dF/dx$ by 10% at most (L05). For f_e estimated on a reef flat, a simple model accounted for refraction and estimated that up to 20%–30% of the observed $-dF/dx$ could be due to refraction (Falter et al. 2004). For observations in deeper water (5–20 m), Snell's law was applied to offshore directional measurements, assuming alongshore uniform bathymetry, to estimate wave angles at shallower sites with the result that wave directional effects on f_e were small (Monismith et al. 2015; R16; G20). On a reef flat in < 1.5 -m water depth, unidirectional waves were assumed (L16). On a fore reef with spur-and-groove formations, wave dissipation estimates between ADCPs incorporated the direct measurements of mean wave direction (Acevedo-Ramirez et al. 2021).

However, waves generally have variable incidence angles and are directionally spread. In our study, the mean angles at B03 in 21-m water depth vary from -30° to -40° (Fig. 3c) and are directionally spread. Thus, the cross-shore energy flux F_x [(8a)] is smaller than F [(10a)], and f_e estimated from dF/dx

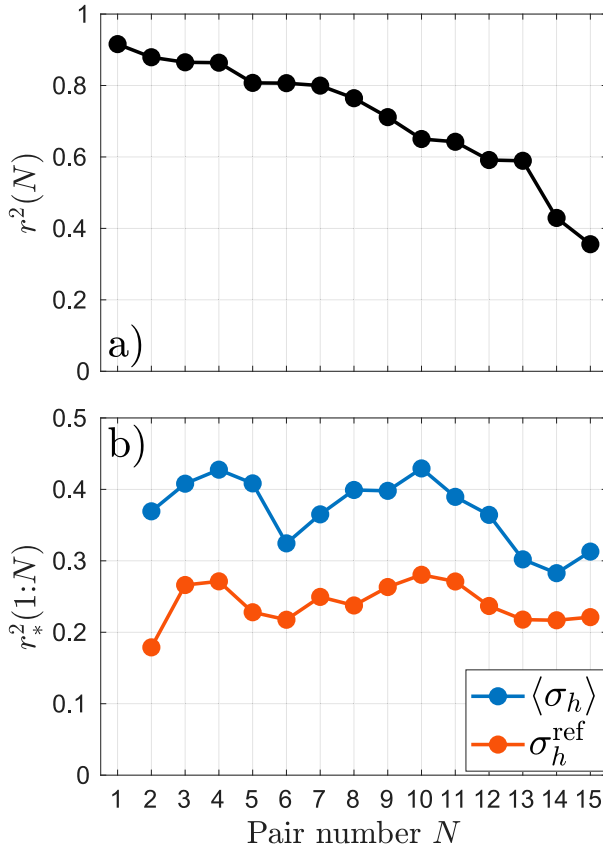


FIG. 8. (a) Correlation coefficient squared r^2 between $\langle U_{\text{rms}} \rangle^3$ and $-dF/dx$ vs instrument pair number N passing primary quality control criteria. Results are sorted by largest to smallest r^2 , as provided in Table 1. (b) The r_*^2 between $\log_{10}(f_e)$ and $\log_{10}(A_b)/\langle \sigma_h \rangle$ (blue) and between $\log_{10}(f_e)$ and $\log_{10}(\langle A_b \rangle / \sigma_h^{\text{ref}})$ (orange) for all pairs up to pair number N .

will have a positive bias. However, mean wave angles at B03 are generally $|\theta_{\text{mean}}| < 20^\circ$ (Fig. 3c), and as (neglecting wave directional spread) $\bar{a}_1 \approx \cos(\theta_{\text{mean}})$ and $\cos(20^\circ) = 0.94$, the bias introduced by neglecting directional wave effects is relatively small.

We examine this bias by estimating the cross-shore energy flux F_x at locations where ADCPs were deployed. We do not estimate F_x at Spotter wave buoys as the directional information, particularly in the swell band, is noisy (C. O. Collins et al. 2024). First, directional moments $a_1(f)$ and $b_1(f)$ were computed with (A2) and (A3) based on velocities measured at bins 0.5–1.6 m above the ADCP transducer. Bulk cross-shore F_x and alongshore F_y wave energy fluxes were computed from (8a) and (8b). From our measurements of dF/dx between adjacent sensors, no pairs of ADCPs yielded large r^2 that indicates a reliable f_e estimate. By considering pairs of nonadjacent instruments, data from two ADCP pairs (B11-B13 and B13-B15, Fig. 5a) can be used to compute f_e from the gradient in F_x . The two pairs satisfy the cross-shore spacing criterion, with $\Delta x = 60$ m and $\Delta x = 92$ m, as well as the other primary quality control criteria (section 3d). At these pairs, the gradients of the total flux $-dF/dx$ and of the cross-shore flux

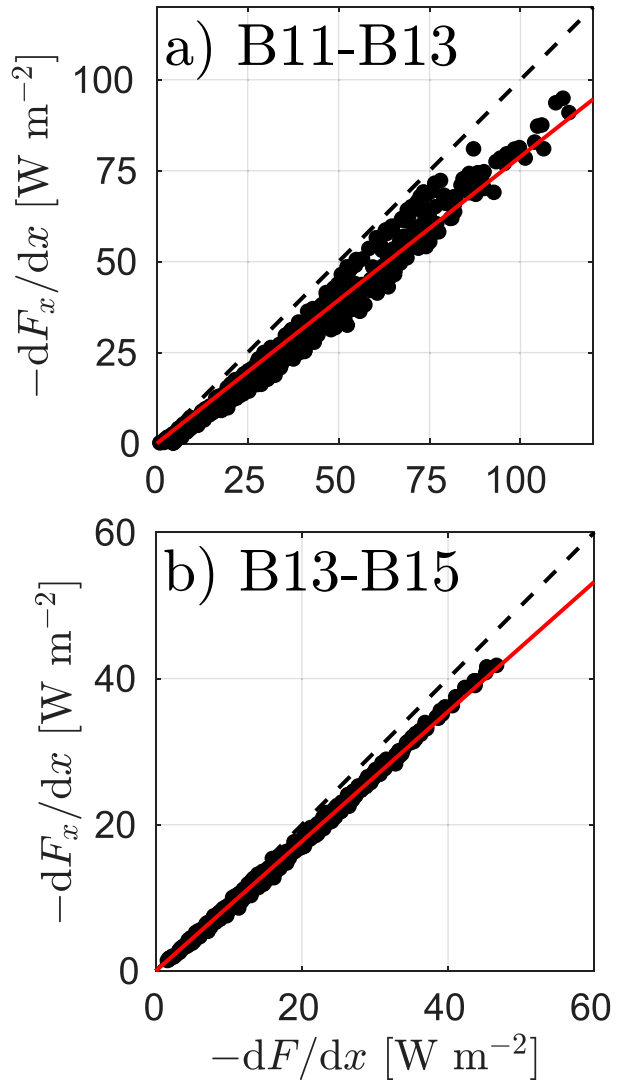


FIG. 9. Scatterplots of the gradients in total flux F (abscissa) and cross-shore flux F_x (ordinate) at two instrument pairs. Cross-shore gradient of the total wave energy flux $-dF/dx$ assuming normally incident waves [(10a)] vs the cross-shore gradient in the cross-shore wave energy flux $-dF_x/dx$ accounting for directional information [(8a)] for instrument pairs (a) B11-B13 and (b) B13-B15. The red solid line is the best-fit linear relationship, and the black dashed line is the 1-to-1 line.

$-dF_x/dx$ are highly correlated, where the correlation coefficient squared is greater than 0.98 (Fig. 9). Generally, $-dF_x/dx$ is smaller than $-dF/dx$ with a best-fit slope of 0.79 and 0.89 at B11-B13 and B13-B15, respectively, implying that using dF/dx overestimates the wave dissipation by 12%–27%. Larger $-dF/dx$ and $-dF_x/dx$ are observed at the deeper B11-B13 than in the shallower B13-B15 as wave dissipation decreases the wave energy flux onshore. At these two locations, we also calculate the bulk friction factor \tilde{f}_e using both dF/dx and dF_x/dx . At both pairs, the correlation squared between $\langle U_{\text{rms}} \rangle^3$ and either dF/dx or dF_x/dx was $r^2 \approx 0.9$, indicating low noise in estimating f_e . At the B11-B13 pair, the bulk

friction factor using $-dF/dx$ is $\tilde{f}_e = 3.2$, whereas using $-dF_x/dx$ results in a reduced $\tilde{f}_e = 2.6$. Similarly, at B13-B15, $\tilde{f}_e = 1.5$ using $-dF/dx$ and $\tilde{f}_e = 1.3$ using $-dF_x/dx$. These changes in \tilde{f}_e are consistent with the changes between $-dF/dx$ and $-dF_x/dx$ (Fig. 9b). Overall, this suggests that using dF/dx results in a 15%–25% positive bias in friction factor estimates. Even when accounting for this potential bias, the observed bulk \tilde{f}_e (Table 1) are still primarily larger than 1.

b. Challenges of intercomparing results with previous studies

Observational and methodological differences in wave friction factor studies can impact the intercomparison of f_e results. For example, different studies have computed the standard deviation of bottom depth σ_h in different ways due to the available bathymetry data. Hereafter, we drop the $\langle \cdot \rangle$ notation. On a coral reef, L05 report σ_h computed within horizontal scales of 0.4–2 m (Nunes and Pawlak 2008). Given the approximately spatially homogeneous bed roughness in their study site, L05 averaged σ_h across their entire instrument array and used a single $\sigma_h = 0.035$ m at the locations where f_e was estimated. Monismith et al. (2015) and R16 did not provide information about σ_h for their measurements over coral reefs. L16 computed a standard deviation of $\sigma_h = 0.13$ m across a single bathymetry transect on a reef flat between one pair of instruments where f_e was estimated. On a coral reef, S23 computed σ_h between 0.08 and 0.15 m within horizontal scales of 0.1–5 m from bathymetry transects (Sous et al. 2020), and used different σ_h for each of three instrument pairs where wave dissipation was measured. On a rocky seabed, G20 computed f_e for one instrument pair and estimated $\sigma_h = 0.9$ m from deviations of bed elevation relative to an alongshore-averaged bathymetry. Here, on a rocky seabed, σ_h was estimated over horizontal scales less than 20 m and typically larger than 1–4 m (section 2b), which are longer length scales than other σ_h estimates by L05 and S23. Across 15 instrument pairs, we computed $0.53 \leq \sigma_h \leq 1.11$ m (Table 1), which is comparable to G20, and much larger than estimates over coral reefs. Apart from S23, other studies did not use variable σ_h between multiple instrument pairs. Overall, the difficulty of bathymetry mapping over rough seabeds leads to differences in how σ_h is computed. Therefore, although rocky shores tend to have significantly larger σ_h , differences in the dependency of f_e on σ_h across studies may be partly due to how σ_h is calculated.

Another intercomparison challenge is the different f_e estimation methods. Friction factors have been computed from frequency-dependent or frequency-integrated energy flux gradients, and reported results include time series of f_e , time-averaged f_e , as well as \tilde{f}_e . From a frequency-dependent energy flux gradient, L05 estimated a frequency-dependent f_e and an hourly energy-weighted f_e , and then time-averaged over the experiment duration. Monismith et al. (2015) and Acevedo-Ramirez et al. (2021) estimated \tilde{f}_e from the frequency-integrated energy flux over fore reefs, and noted the high correlation ($r^2 = 0.83$ and $r^2 = 0.9$, respectively) between $-dF/dx$ and $\langle U_{\text{rms}} \rangle^3$. R16 followed a similar approach to Monismith et al. (2015), but estimated time-dependent f_e at three regions around an atoll. L16

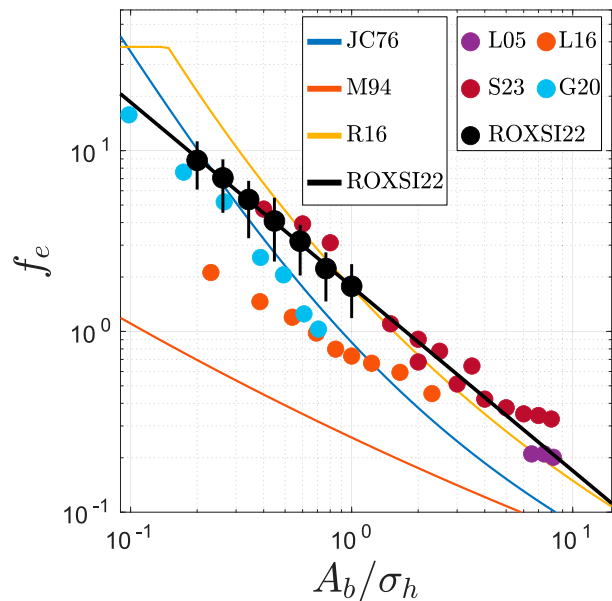


FIG. 10. Bin-averaged f_e vs A_b/σ_h from the ROXSI 2022 observations (black dots) and the power-law (black line) relationship [(15)]. Observations from previous field experiments are taken from L05, L16, G20, and S23, where correction factors have been multiplied to results to make definitions of f_e consistent (appendix B). Curves indicate parameterizations of f_e taken from the literature (appendix C) and normalized by correction factors in appendix B: JC76, M94, and R16. These parameterizations are based on A_b/k_N , and it was assumed that $k_N = 4\sigma_h$ to plot f_e vs A_b/σ_h .

also estimated time series of f_e from sea-swell-integrated dissipation. G20 computed hourly friction factors and, although their results show f_e decreasing with A_b , large f_e noise around their bin means are evident. S23 used a spectral wave action balance, including nonlinear energy transfers and wave–current interactions, to compute a frequency-dependent friction factor at each hour across a reef flat, and their frequency-integrated f_e have small deviations from binned means as a function of A_b . In our study, frequency-integrated energy flux gradients across 33 instrument pairs were used to compute f_e . Quality control criteria yielded 15 instrument pairs (Table 1) where f_e was estimated, and results were sorted to retain 10 pairs with the highest signal-to-noise ratio inferred from r^2 (Fig. 7). Furthermore, wave dissipation D_f has variable definitions yielding inconsistent f_e and requiring rescaling for a consistent intercomparison (see appendix B).

c. Intercomparison with previous studies and parameterizing f_e

We now intercompare our results from the ROXSI 2022 experiment with previous field observations on rocky seabeds and coral reefs (Fig. 10). Friction factors from different studies were scaled to account for different definitions of f_e (see appendix B). For consistency with the dissipation [(12)], f_e from L05 and S23 were multiplied by 0.875, and f_e of L16 and G20 were multiplied by 0.5 (appendix B). Results from L05 were taken between three instrument pairs and represent

a time average (over the experiment duration) of the representative friction factor in their spectral model. Both L16 and G20 computed f_e between one instrument pair in their experiments, and results were individually bin averaged in A_b/σ_h . Observations by S23 yield f_e between three instrument pairs, and the time series of the representative friction factor in their spectral model were bin averaged at each pair independently. We did not intercompare with results from additional field experiments (Monismith et al. 2015; R16; Acevedo-Ramirez et al. 2021) because σ_h was not provided.

Results from ROXSI 2022 cover a wide range of water depths from several instrument pairs, typically within $10 \leq \bar{h} \leq 3$ m, with large σ_h (0.7–1.1 m) and A_b (0.15–0.7 m) (Table 1). Our binned-mean f_e estimates are primarily between 2 and 10 for $0.2 \leq A_b/\sigma_h \leq 1$ (black dots in Fig. 10). From an experiment at a different site on the Monterey Peninsula, G20 estimated binned-mean $1 < f_e < 20$ (red dots, Fig. 10) that are smaller than our results for the same A_b/σ_h with a steeper power-law slope. These results are based on two measurements around $8 \leq \bar{h} \leq 6$ m, with similar σ_h and A_b than those in ROXSI 2022. When considering multiple experiments on coral reefs (L05; L16; S23), observations of wave dissipation cover a wider range of A_b/σ_h , i.e., from 0.2 to 10, than measurements over rocky seabeds that have $A_b/\sigma_h \leq 1$. For small $A_b/\sigma_h \leq 1$, binned-mean friction factor estimates on coral reefs range from 0.7 to 5, and f_e decrease to 0.2 at large $A_b/\sigma_h \approx 10$. For $A_b/\sigma_h \leq 1$, our binned-mean f_e over a rocky seabed are similar to observations on coral reefs by S23. The binned-mean f_e from L16 are a factor 3–4 smaller than our results for similar A_b/σ_h . We also note that similar A_b/σ_h values have distinct A_b and σ_h between rocky seabeds and coral reefs. Small A_b/σ_h on coral reefs typically have both σ_h and A_b smaller than those on rocky seabeds by a factor of 2–5, based on observations from shallow reef flats (i.e., $\bar{h} < 2$ m, L16; S23) or fore reefs, located in deeper water depths (i.e., $5 \leq \bar{h} < 20$ m, Monismith et al. 2015; R16).

Parameterizations of f_e are usually expressed in terms of the roughness parameter k_N (appendix C). For applying parameterizations to $A_b/k_N \leq 1$, it has been suggested (L05; S23; Dealbera et al. 2024) that $k_N \approx 4\sigma_h$. Using $\sigma_h = k_N/4$, we evaluate existing f_e parameterizations in terms of A_b/σ_h (Fig. 10). We note that these parameterizations were developed for $A_b/k_N \gg 1$, or equivalently for $A_b/\sigma_h \gg 4$; thus, technically, the assumptions built into the f_e parameterizations are violated. Parameterizations from JC76 and R16 roughly predict the magnitude of the binned-mean f_e from most experiments, but the relationship between f_e and A_b/σ_h tends to have a steeper slope than in the observations. Several experiments have significantly larger f_e than the maximum friction factor of 0.3 in the parameterization by Madsen et al. (1988) (not shown), which is a standard formulation implemented in numerical wave models (Booij et al. 1999). Although the coefficients in the parameterization from M94 have been modified to yield a best fit to f_e observations (L05; S23; Dealbera et al. 2024), the expression taken directly from M94 yields much smaller friction factors than the observations.

Our observations indicate that a power-law parameterization for f_e in terms of A_b/σ_h can be used to model wave

transformation over rough seabeds with $0.2 \leq A_b/\sigma_h \leq 1$. Based on the 10 instrument pairs with $r^2 \geq 0.65$ from the ROXSI 2022 experiment (section 3e), a standard least-squared fit to the bin means of $\log_{10}(f_e)$ and $\log_{10}(A_b/\sigma_h)$ (Fig. 7a) yields

$$f_e = 1.77 \left(\frac{A_b}{\sigma_h} \right)^{-1.02}. \quad (15)$$

The power law (15) from our results over a rocky seabed yields similar f_e than observations from S23 and L05 over coral reefs. The agreement between these results and (15) is within a factor of 2, even for A_b/σ_h up to 10, which is well beyond the regime of our observations. The power law overestimates friction factors from L16 by a factor of 3–4, as well as from G20 for $A_b/\sigma_h > 0.5$, which could be associated with different methodologies (section 4b) or the importance of incorporating seabed statistics in addition to σ_h (Dealbera et al. 2024). Based on parameterizations for $A_b/\sigma_h \gg 1$ (e.g., JC76), the power law (15) will underestimate the friction factor for the smaller roughness of sandy seabeds, such that our parameterization is not valid for very large A_b/σ_h . Nevertheless, the power law (15) provides a simple and practical estimate of f_e within $0.2 \leq A_b/\sigma_h \leq 10$, which is in good agreement with some previous field experiments and can be used to calculate wave dissipation over environments with a rough seabed.

Similar to coral reef measurements, (15) supports that the gradient of f_e with A_b/σ_h is smaller than predicted from expressions like from JC76 or R16. A power of -1 is in agreement with laboratory studies using roughness elements with length scales between 0.5 and 1.3 cm (Mirfenderesk and Young 2003), and those using stones and ping-pong balls with sizes of approximately 1.5–4 cm (Dixen et al. 2008). Therefore, extrapolating f_e parameterizations developed for sand grains with $A_b/\sigma_h \gg 1$ may lead to errors in wave dissipation over rough bathymetry, and (15) is more suitable for wave modeling over coral reefs and rocky seabeds.

5. Summary and conclusions

We presented observations from a month-long experiment, the first field campaign of the Rocky Shores: Experiment and Simulations (ROXSI). Specifically, we examined the cross-shore wave transformation from 20-m water depth to the shoreline at two sites on the rocky shore of the Monterey Peninsula, California, United States. The directly measured seabed was rough with a large standard deviation of bed elevation σ_h of 0.5–1.5 m. The incident significant wave height varied from 0.3 to 2 m. Significant wave height and cross-shore sea-swell wave energy flux decay onshore of 8-m water depth. These depths are well offshore of the surfzone suggesting that the sea-swell wave energy is attenuated due to bottom friction. Incident mean wave angles in 20-m water depth were largely within $\pm 20^\circ$ and refracted toward normal incidence in shallower water.

Friction factors f_e were estimated between instrument pairs balancing the cross-shore sea-swell energy flux gradient with the parameterized wave dissipation $D_f = 0.8\rho f_e U_{\text{rms}}^3$, where

we computed U_{rms} from pressure measurements and linear-wave theory, and we assumed normally incident waves. Quality control criteria were applied to neglect instrument pairs where f_e estimates were not reliable. Fifteen instrument pairs pass the primary quality control criteria with large bulk friction factors varying between 1.0 and 5, among the largest friction factors reported on coral reefs and rocky shores. Additionally, the squared correlation r^2 between the observed flux convergence $-dF/dx$ and the cubed bottom orbital velocity $\langle U_{\text{rms}} \rangle^3$ is used as an additional quality control constraint. Ten instrument pairs have $r^2 \geq 0.65$, and their resulting hourly f_e vary between 1 and 10. For these 10 instrument pairs, the hourly f_e consistently increase with smaller A_b/σ_h , the ratio of the orbital amplitude A_b to the standard deviation of seabed elevation σ_h . In log space, f_e and A_b/σ_h are correlated with a maximum $r_*^2 = 0.43$, and binned means of f_e indicate a power-law scaling with A_b/σ_h . We also related f_e to a constant $\sigma_h^{\text{ref}} = 0.8\text{m}$ (i.e., the mean σ_h across instrument sites), which reduces r_*^2 to 0.28. Although r_*^2 depends on the number of instrument pairs used when computing r_*^2 , the reduction when using σ_h^{ref} instead of σ_h is a robust result. This decrease in r_*^2 demonstrates that our estimate of σ_h is a good proxy for the roughness of the seabed, with larger σ_h enhancing f_e .

Our results are broadly consistent with previous observations of large f_e on coral reefs and rocky shores, and potential sources of discrepancies between studies are discussed. Binned means of f_e range from 2 to 10 in the ROXSI observations, while previous studies have f_e between 0.7 and 8 for $0.2 \leq A_b/\sigma_h \leq 1$. Although our estimates are based on the assumption of normally incident waves, directly measured mean wave angles and directional fluxes at a few locations yield a relatively small (15%–25%) reduction in f_e . While statistics of seabed variability other than σ_h might be needed to intercompare results, different methodologies across studies for computing f_e and σ_h might also contribute to discrepancies. Nevertheless, f_e across studies are broadly consistent with a scaling with A_b/σ_h that has a lower slope than predicted by parameterizations developed for small-scale ($A_b/k_N \gg 1$) roughness. The ROXSI observations, based on measurements from a large number of 10 instrument pairs and spanning a wide range of water depths between 3 and 10 m, yield an empirical power law for f_e in terms of A_b/σ_h , where the power-law exponent is approximately -1 . Given this empirical parameterization for f_e , along with high-resolution bathymetry, wave dissipation can be parameterized over the highly rough ($A_b/\sigma_h \leq 1$) seabeds of coral reefs and rocky shores.

Acknowledgments. This paper is part of the Rocky Shore: Experiment and Simulations (ROXSI) project, funded by the Office of Naval Research through Grants N000142112786 and N0001423WX01357. The Monterey NOAA Sanctuary, CA Fish and Wildlife, Pebble Beach, and Pacific Grove provided environmental permission for the experiment, and we thank Chris Miller at NPS for support with the permitting process. We thank scientists, students, and technical personnel from

SIO, NPS, UNCW, OSU, and UNC-Chapel Hill for their invaluable support with the field experiment; for SIO: Brian Woodward, Kent Smith, Rob Grenzeback, Lucian Parry, Shane Finnerty, Carson Black, Duncan Wheeler, Annie Adelson, Loren Clark, Kaden Quinn, and Kanoa Pick; for NPS: Paul Jessen, Charlotte Benbow, Pat Collins, Mike Cook, Matt Gough, and Ian Jenstrom; for UNCW: Tim Hesford; for OSU: Greg Wilson, Matt Conlin, and June Marion; and for UNC-Chapel Hill: Johanna Rosman, Mika Malila, and Anthony Whipple. We are grateful to Steve Lentz, Justin Rogers, and Damien Sous for sharing their data with us. We thank Stephen Monismith for sharing his notes, which we strongly borrowed from in [appendix B](#), and for pointing out that correction factors are necessary to intercompare friction factors between different studies. OBM appreciates discussions with Matt Conlin and Kaden Quinn. We thank the questions and comments from two reviewers, which helped to improve the manuscript.

Data availability statement. The data presented in this paper are available as a Zenodo dataset repository at <https://doi.org/10.5281/zenodo.15199472> (Marques et al. 2025). MATLAB code for reproducing the data processing and figures is available at the GitHub repository github.com/olavobm/Paper_Wave_Dissipation.

APPENDIX A

Sea-Swell Mean Period and Mean Direction

From the sea surface elevation spectrum S_η , the sea-swell mean wave period is computed as

$$T_{\text{mean}} = \frac{\int_{\text{SS}} S_\eta df}{\int_{\text{SS}} f S_\eta df}. \quad (\text{A1})$$

Either sea surface displacements from wave buoys or pressure and horizontal velocity measurements from ADCPs can be used to calculate standard directional surface wave moments and statistics (e.g., Longuet-Higgins et al. 1963; Kuik et al. 1988; Thomson et al. 2018). For example, directional wave moments can be computed from the x , y , and z components of sea surface displacement, in terms of their spectra [$S_x(f)$, $S_y(f)$, and $S_z(f)$, respectively] and their cross-spectra. The first directional moments are computed as

$$a_1(f) = \frac{-Q_{xz}}{\sqrt{S_z(S_x + S_y)}}, \quad (\text{A2})$$

$$b_1(f) = \frac{-Q_{yz}}{\sqrt{S_z(S_x + S_y)}}, \quad (\text{A3})$$

where $Q_{xz}(f)$ and $Q_{yz}(f)$ are the quadrature spectra (i.e., minus the imaginary part of the cross-spectra) between x and z and between y and z , respectively.

The sea-swell directional moments are computed from energy-weighted averages in frequency space of (A2) and (A3). For example,

$$\bar{a}_1 = \frac{\int_{SS} a_1 S_\eta df}{\int_{SS} S_\eta df}, \quad (\text{A4})$$

where the subscript SS denotes the 0.05–0.2-Hz frequency range used throughout this paper for the sea-swell band. The mean direction θ_{mean} was computed as

$$\theta_{\text{mean}} = \tan^{-1}\left(\frac{\bar{b}_1}{\bar{a}_1}\right), \quad (\text{A5})$$

which, along with definitions (A2) and (A3), corresponds to the direction of wave propagation relative to the cross-shore (+x).

APPENDIX B

Wave Dissipation Parameterized by f_e

We compared f_e from previous field measurements (L05; L16; G20; S23) with our results from the ROXSI 2022 experiment (Fig. 10). However, different definitions have been used to express the dissipation in terms of f_e for the various experiments. Here, we examine the f_e definition across studies and present scaling factors (Table B1) to make previous results consistent with our results and (12). Much of this appendix borrows from notes by Prof. Stephen Monismith of Stanford University, to whom we are grateful. The wave energy dissipation factor f_e , which we and others (e.g., L16) commonly refer to as wave friction factor, is defined in terms of the wave energy dissipation D_f as

$$D_f = \rho \frac{f_e}{2} \overline{u^2 |u|}, \quad (\text{B1})$$

where the overbar is a time average and u is the horizontal velocity assuming unidirectional wave propagation. For field observations, u is taken as the horizontal velocity evaluated at the seabed from potential flow wave theory (e.g., L16). For a monochromatic velocity $u = U_0 \cos(\omega t)$, (B1) yields

$$D_f = \rho \frac{f_e}{2} U_0^3 \overline{\cos^2(\omega t) |\cos(\omega t)|} = \frac{2}{3\pi} \rho f_e U_0^3 \approx 0.21 \rho f_e U_0^3, \quad (\text{B2})$$

and with $U_{\text{rms}} = \sqrt{\overline{u^2}} = U_0/\sqrt{2}$, wave dissipation [(B2)] becomes

$$D_f \approx (0.21 \times 2\sqrt{2}) \rho f_e U_0^3 \approx 0.6 \rho f_e U_{\text{rms}}^3. \quad (\text{B3})$$

JC76 and R16 used (B3) to relate f_e to D_f .

Wave dissipation can also be written in terms of wave height H through linear theory. The peak horizontal velocity at the bottom is related to H by (e.g., Dean and Dalrymple 1991)

TABLE B1. Reference with abbreviation, application type (field data or parameterization), equation representing wave dissipation, and constant multiplied by f_e to make f_e estimates consistent with (B1).

Reference	Type	Equation	Constant
L05	Field data	(B14)	0.875
L16	Field data	(B12)	0.5
G20	Field data	(B15)	0.5
S23	Field data	(B14)	0.875
JC76	Parameterization	(B3)	0.75
M94	Parameterization	(B14)	0.875
R16	Parameterization	(B3)	0.75

$$U_0 = \frac{\omega}{\sinh(kh)} \frac{H}{2}, \quad (\text{B4})$$

where ω is the radian frequency, h is the water depth, and k is the wavenumber evaluated from the dispersion relationship [(3)]. Substituting (B4) into (B3) yields

$$D_f = \frac{1}{12\pi} \rho f_e \left[\frac{\omega}{\sinh(kh)} \right]^3 H^3. \quad (\text{B5})$$

Considering a narrow-band random wave field, wave dissipation becomes (Thornton and Guza 1983)

$$D_f = \frac{1}{12\pi} \rho f_e \left[\frac{\omega_{\text{mean}}}{\sinh(k_{\text{mean}} h)} \right]^3 \int_0^\infty H^3 p(H) dH, \quad (\text{B6})$$

where ω_{mean} is the mean wave frequency, k_{mean} is the wavenumber correspondent to ω_{mean} , and $p(H)$ is the Rayleigh probability density function:

$$p(H) = \frac{2H}{H_{\text{rms}}^2} \exp\left[-\left(\frac{H}{H_{\text{rms}}}\right)^2\right]. \quad (\text{B7})$$

Expression [(B6)] is equivalent to the dissipation $\langle \epsilon_f \rangle$ in Thornton and Guza (1983), who used the coefficient $c_f \equiv f_e/2$. The integral in (B6) is

$$\int_0^\infty H^3 p(H) dH = \frac{3\sqrt{\pi}}{4} H_{\text{rms}}^3, \quad (\text{B8})$$

resulting in

$$D_f = \frac{1}{16\sqrt{\pi}} \rho f_e \left[\frac{\omega_{\text{mean}}}{\sinh(k_{\text{mean}} h)} \right]^3 H_{\text{rms}}^3. \quad (\text{B9})$$

Thornton and Guza (1983) missed a factor of 2 when evaluating (B8), such that (B9) is twice their Eq. (40) for energy dissipation (Thornton and MacMahan 2024). For a narrow-band wave field,

$$U_{\text{rms}} = \frac{\omega_{\text{mean}}}{\sinh(k_{\text{mean}} h)} \frac{H_{\text{rms}}}{2\sqrt{2}}, \quad (\text{B10})$$

and substituting (B10) into (B9) yields

$$D_f = \sqrt{\frac{2}{\pi}} \rho f_e U_{\text{rms}}^3 \approx 0.8 \rho f_e U_{\text{rms}}^3, \quad (\text{B11})$$

which is equivalent to (12) that we applied to parameterize dissipation in this paper. The dissipation from L16 can be written as

$$D_f \approx 0.4 \rho f_e U_{\text{rms}}^3, \quad (\text{B12})$$

which differs from (B11) by a factor of 2 because the correction to Thornton and Guza (1983) was not implemented.

M94, L05, and S23 parameterized the spectral wave energy dissipation \mathcal{D}_f in terms of the spectrum of wave horizontal velocity denoted as $S_u(\omega)$. The dissipation \mathcal{D}_f was parameterized as

$$\mathcal{D}_f(\omega) = \frac{1}{4} \rho f_e(\omega) u_{b,r} u_b^2(\omega), \quad (\text{B13})$$

where $u_b(\omega) = \sqrt{2S_u(\omega)}$, and $u_{b,r} = \sqrt{\int u_b^2(\omega) d\omega} = \sqrt{2} U_{\text{rms}}$ is the representative wave velocity as defined by M94. In terms of S_u and $U_{\text{rms}} = \sqrt{\int S_u d\omega}$, (B13) can be rewritten as

$$\mathcal{D}_f(\omega) = \frac{\sqrt{2}}{2} \rho f_e(\omega) U_{\text{rms}} S_u(\omega). \quad (\text{B14})$$

G20 also parameterized dissipation spectrally, but used

$$\mathcal{D}_f(\omega) = \frac{\sqrt{2}}{2\sqrt{\pi}} \rho f_e U_{\text{rms}} S_u(\omega), \quad (\text{B15})$$

where f_e is not a function of frequency, and the coefficient is the same as in (B12). For a narrow-band wave spectrum, the integral of $\mathcal{D}_f(\omega)$ over the sea-swell band of (B14) or (B15) yields a dissipation D_f that can be compared with (B11). For the f_e intercomparison (Fig. 10), f_e from other studies were multiplied by the appropriate constants (Table B1) to make all results consistent with (B11).

APPENDIX C

Wave Friction Factor Parameterizations

Several parameterizations for the wave friction factor have been derived for large A_b/k_N , and three solutions are shown in Fig. 10. Here, we present the f_e parameterizations shown in Fig. 10. The wave friction factor f_w in boundary layer theory relates the bottom shear stress to the velocity above the boundary layer (e.g., Jonsson 1966). Measurements of the velocity profile within the boundary layer yield the hydraulic roughness z_0 , and $k_N \equiv 30z_0$. JC76 presented the semiempirical parameterization for f_w as follows:

$$\frac{1}{4\sqrt{f_w}} + \log_{10} \frac{1}{4\sqrt{f_w}} = 0.20 + \log_{10} \frac{A_b}{k_N}, \quad (\text{C1})$$

that is valid for $A_b/k_N \gg 1$. Parameterization (C1) is semiempirical because the form of the equation is theoretically derived for a rough turbulent boundary layer under a monochromatic wave, but the first term on the right-hand side is a coefficient that must be computed from laboratory measurements (JC76). Based on earlier laboratory experiments,

Jonsson (1966) obtained a coefficient of -0.08 instead of 0.20 . For practical purposes, Swart (1974) approximated the f_w solution from Jonsson (1966) as

$$f_w = \exp \left[5.213 \left(\frac{A_b}{k_N} \right)^{-0.194} - 5.977 \right], \quad (\text{C2})$$

which is accurate to within 3% of the full solution for $A_b/k_N > 1$, but diverges for $A_b/k_N < 1$. R16 implemented (C2) in a wave model, but with a maximum of $f_w = 50$ for $A_b/k_N < 0.0369$ to avoid unrealistically large f_w . Nielsen (1992) adjusted the coefficients in (C2) to improve agreement with laboratory measurements in the regime of $A_b/k_N \gg 1$. In Fig. 10, the parameterization JC76 was computed from (C1), and R16 from (C2) with the cutoff $f_w = 50$. Both parameterizations were then normalized according to Table B1. The assumption $f_e = f_w$ was used in Fig. 10, which is commonly assumed for rough turbulent boundary layers (Nielsen 1992).

Grant and Madsen (1979) derived a fully theoretical solution for f_w in a model that includes the combined effect of a current and a monochromatic wave. M94 extended the Grant and Madsen (1979) model for a wave spectrum and, based on the approach from Swart (1974), the approximate solution for f_w (without a mean flow) was given as

$$f_w(\omega_r) = \exp \left[7.02 \left(\frac{u_{b,r}}{k_N \omega_r} \right)^{-0.078} - 8.82 \right], \quad (\text{C3})$$

where $u_{b,r}$ is the same representative velocity as in (B13) and ω_r is the representative wave frequency, defined as the mean radian frequency. M94 reports that (C3) is a valid approximation to the full solution of his model within $0.2 \leq u_{b,r}/(k_N \omega_r) \leq 100$. Interestingly, M94 claims that his solution is valid for large-scale roughness $u_{b,r}/(k_N \omega_r) \leq 1$. In the absence of a mean flow, the wave energy dissipation in the model by M94 is given by (B13), where f_w and f_e were related through

$$f_e = f_w \cos(\Theta), \quad \Theta(\omega_r) = 33 - 6.0 \log_{10} \left(\frac{u_{b,r}}{k_N \omega_r} \right), \quad (\text{C4})$$

where Θ is in degrees. M94 stated that, for $0.2 \leq u_{b,r}/(k_N \omega_r) \leq 1000$, the approximation (C4) is accurate to within 1% of the full solution.

Both L05 and S23 cited M94 to compare their observed f_e with theory and to compute k_N . L05 used a spectral f_e parameterization with the same form as (C3) and (C4), but with the coefficients that Nielsen (1992) modified from Swart (1974). S23 followed M94, including the effect of the mean flow, but all the coefficients in (C3) were changed to provide a best fit to the observations. Since (C3) and (C4) are based on a fully theoretical model, the coefficients in (C3) should not be changed, and L05 and S23 did not apply M94's model. Given that the coefficients in the expressions used by L05 and S23 are based on an adjustment of the parameterizations to observations, the model by M94 does not agree with measurements for $A_b/k_N < 20$ (Fig. 10). The f_e denoted as M94 in Fig. 10 was computed from (C3) and (C4) after substituting $A_b = u_{b,r}/\omega_r$ and $k_N = 4\sigma_b$, as suggested by L05 and S23. The M94 parameterization was normalized according to Table B1.

REFERENCES

- Acevedo-Ramirez, C. A., W. Stephenson, S. Wakes, and I. Mariño-Tapia, 2021: Wave transformation on a fringing reef system with spur and groove structures. *J. Geophys. Res. Oceans*, **126**, e2020JC016910, <https://doi.org/10.1029/2020JC016910>.
- Amador, A., I. B. Arzeno, S. N. Giddings, M. A. Merrifield, and G. Pawlak, 2020: Cross-shore structure of tidally driven along-shore flow over rough bathymetry. *J. Geophys. Res. Oceans*, **125**, e2020JC016264, <https://doi.org/10.1029/2020JC016264>.
- Barnard, P. L., L. H. Erikson, and R. G. Kvitck, 2011: Small-scale sediment transport patterns and bedform morphodynamics: New insights from high-resolution multibeam bathymetry. *Geo-Mar. Lett.*, **31**, 227–236, <https://doi.org/10.1007/s00367-011-0227-1>.
- Barr, B. C., D. N. Slinn, T. Pierro, and K. B. Winters, 2004: Numerical simulation of turbulent, oscillatory flow over sand ripples. *J. Geophys. Res.*, **109**, C09009, <https://doi.org/10.1029/2002JC001709>.
- Bishop, C. T., and M. A. Donelan, 1987: Measuring waves with pressure transducers. *Coastal Eng.*, **11**, 309–328, [https://doi.org/10.1016/0378-3839\(87\)90031-7](https://doi.org/10.1016/0378-3839(87)90031-7).
- Booij, N., R. C. Ris, and L. H. Holthuijsen, 1999: A third-generation wave model for coastal regions: 1. Model description and validation. *J. Geophys. Res.*, **104**, 7649–7666, <https://doi.org/10.1029/98JC02622>.
- Chung, D., N. Hutchins, M. P. Schultz, and K. A. Flack, 2021: Predicting the drag of rough surfaces. *Annu. Rev. Fluid Mech.*, **53**, 439–471, <https://doi.org/10.1146/annurev-fluid-062520-115127>.
- Collins, C. O., and Coauthors, 2024: Performance of moored GPS wave buoys. *Coastal Eng. J.*, **66**, 17–43, <https://doi.org/10.1080/21664250.2023.2295105>.
- Collins, P., J. MacMahan, E. Thornton, C. Benbow, and P. Jessen, 2024: Beach and backward Bragg sea-swell wave reflection across rocky and sandy shores. *J. Geophys. Res. Oceans*, **129**, e2023JC020177, <https://doi.org/10.1029/2023JC020177>.
- CSUMB, and Seafloor Mapping Laboratory, 2014: California Seafloor Mapping Project – Undersea Imagery Archive 2007–2014. Accessed 10 April 2022, <https://csumb.edu/undersea/seafloor-maps>.
- Dalrymple, R. A., J. H. MacMahan, A. J. Reniers, and V. Nelko, 2011: Rip currents. *Annu. Rev. Fluid Mech.*, **43**, 551–581, <https://doi.org/10.1146/annurev-fluid-122109-160733>.
- Davis, K. A., G. Pawlak, and S. G. Monismith, 2021: Turbulence and coral reefs. *Annu. Rev. Mar. Sci.*, **13**, 343–373, <https://doi.org/10.1146/annurev-marine-042120-071823>.
- Dealbera, S., D. Sous, D. Morichon, and H. Michaud, 2024: The role of roughness geometry in frictional wave dissipation. *Coastal Eng.*, **189**, 104478, <https://doi.org/10.1016/j.coastaleng.2024.104478>.
- Dean, R. G., and R. A. Dalrymple, 1991: *Water Wave Mechanics for Engineers and Scientists*. Vol. 2. World Scientific Publishing Company, 368 pp.
- Denny, M., 1995: Predicting physical disturbance: Mechanistic approaches to the study of survivorship on wave-swept shores. *Ecol. Monogr.*, **65**, 371–418, <https://doi.org/10.2307/2963496>.
- Dixen, M., F. Hatipoglu, B. M. Sumer, and J. Fredsøe, 2008: Wave boundary layer over a stone-covered bed. *Coastal Eng.*, **55** (1), 1–20, <https://doi.org/10.1016/j.coastaleng.2007.06.005>.
- Emery, W. J., and R. E. Thomson, 2014: *Data Analysis Methods in Physical Oceanography*. Elsevier Science, 716 pp.
- Falter, J. L., M. J. Atkinson, and M. A. Merrifield, 2004: Mass-transfer limitation of nutrient uptake by a wave-dominated reef flat community. *Limnol. Oceanogr.*, **49**, 1820–1831, <https://doi.org/10.4319/lo.2004.49.5.1820>.
- Feddersen, F., R. T. Guza, S. Elgar, and T. H. C. Herbers, 1998: Alongshore momentum balances in the nearshore. *J. Geophys. Res.*, **103**, 15667–15676, <https://doi.org/10.1029/98JC01270>.
- Flack, K. A., and M. P. Schultz, 2010: Review of hydraulic roughness scales in the fully rough regime. *J. Fluids Eng.*, **132**, 041203, <https://doi.org/10.1115/1.4001492>.
- Gerritsen, F., 1980: Wave attenuation and wave set-up on a coastal reef. *Coastal Eng.*, **1980**, 444–461, <https://doi.org/10.1061/9780872622647.028>.
- Gon, C. J., J. H. MacMahan, E. B. Thornton, and M. Denny, 2020: Wave dissipation by bottom friction on the inner shelf of a rocky shore. *J. Geophys. Res. Oceans*, **125**, e2019JC015963, <https://doi.org/10.1029/2019JC015963>.
- Grant, W. D., and O. S. Madsen, 1979: Combined wave and current interaction with a rough bottom. *J. Geophys. Res.*, **84**, 1797–1808, <https://doi.org/10.1029/JC084iC04p01797>.
- Guza, R. T., and E. B. Thornton, 1980: Local and shoaled comparisons of sea surface elevations, pressures, and velocities. *J. Geophys. Res.*, **85**, 1524–1530, <https://doi.org/10.1029/JC085iC03p01524>.
- Hardy, T. A., and I. R. Young, 1996: Field study of wave attenuation on an offshore coral reef. *J. Geophys. Res.*, **101**, 14311–14326, <https://doi.org/10.1029/96JC00202>.
- Herbers, T. H. C., S. Elgar, and R. T. Guza, 1994: Infragravity-frequency (0.005–0.05 Hz) motions on the shelf. Part I: Forced waves. *J. Phys. Oceanogr.*, **24**, 917–927, [https://doi.org/10.1175/1520-0485\(1994\)024%3C0917:IFHMOT%3E2.0.CO;2](https://doi.org/10.1175/1520-0485(1994)024%3C0917:IFHMOT%3E2.0.CO;2).
- , —, and —, 1999: Directional spreading of waves in the nearshore. *J. Geophys. Res.*, **104**, 7683–7693, <https://doi.org/10.1029/1998JC900092>.
- , P. F. Jessen, T. T. Janssen, D. B. Colbert, and J. H. MacMahan, 2012: Observing ocean surface waves with GPS-tracked buoys. *J. Atmos. Oceanic Technol.*, **29**, 944–959, <https://doi.org/10.1175/JTECH-D-11-00128.1>.
- Huang, Z.-C., L. Lenain, W. K. Melville, J. H. Middleton, B. Reineman, N. Statom, and R. M. McCabe, 2012: Dissipation of wave energy and turbulence in a shallow coral reef lagoon. *J. Geophys. Res.*, **117**, C03015, <https://doi.org/10.1029/2011JC007202>.
- Jonsson, I. G., 1966: Wave boundary layers and friction factors. *Coastal Engineering 1966*, American Society of Civil Engineers, 127–148, <https://doi.org/10.1061/9780872620087.010>.
- , and N. A. Carlsen, 1976: Experimental and theoretical investigations in an oscillatory turbulent boundary layer. *J. Hydraul. Res.*, **14**, 45–60, <https://doi.org/10.1080/00221687609499687>.
- Kamphuis, J. W., 1974: Determination of sand roughness for fixed beds. *J. Hydraul. Res.*, **12**, 193–203, <https://doi.org/10.1080/00221687409499737>.
- , 1975: Friction factor under oscillatory waves. *J. Waterw., Harbors Coastal Eng. Div.-ASCE*, **101**, 135–144, <https://doi.org/10.1061/AWHCAR.0000276>.
- Kuiik, A. J., G. P. Van Vledder, and L. H. Holthuijsen, 1988: A method for the routine analysis of pitch-and-roll buoy wave data. *J. Phys. Oceanogr.*, **18**, 1020–1034, [https://doi.org/10.1175/1520-0485\(1988\)018%3C1020:AMFTRA%3E2.0.CO;2](https://doi.org/10.1175/1520-0485(1988)018%3C1020:AMFTRA%3E2.0.CO;2).
- Lentz, S. J., J. H. Churchill, K. A. Davis, and J. T. Farrar, 2016: Surface gravity wave transformation across a platform coral reef in the Red Sea. *J. Geophys. Res. Oceans*, **121**, 693–705, <https://doi.org/10.1002/2015JC011142>.
- Longuet-Higgins, M. S., D. E. Cartwright, and N. D. Smith, 1963: Observations of the directional spectrum of sea waves using the motions of a floating buoy. *Ocean Wave Spectra*, Prentice Hall, 111–136.

- Lowe, R. J., J. L. Falter, M. D. Bandet, G. Pawlak, M. J. Atkinson, S. G. Monismith, and J. R. Koseff, 2005: Spectral wave dissipation over a barrier reef. *J. Geophys. Res.*, **110**, C04001, <https://doi.org/10.1029/2004JC002711>.
- , —, J. R. Koseff, S. G. Monismith, and M. J. Atkinson, 2007: Spectral wave flow attenuation within submerged canopies: Implications for wave energy dissipation. *J. Geophys. Res.*, **112**, C05018, <https://doi.org/10.1029/2006JC003605>.
- MacMahan, J., E. Thornton, S. Dressel, and M. Cook, 2024: Intermediate wave scale rocky bottom variability for the near-shore along California. *Earth Space Sci.*, **11**, e2023EA003475, <https://doi.org/10.1029/2023EA003475>.
- Madsen, O. S., 1994: Spectral wave-current bottom boundary layer flows. *Coastal Engineering 1994*, American Society of Civil Engineers, 384–398, <https://doi.org/10.1061/9780784400890.030>.
- , Y.-K. Poon, and H. C. Graber, 1988: Spectral wave attenuation by bottom friction: Theory. *Coastal Engineering 1988*, American Society of Civil Engineers, 492–504, <https://doi.org/10.1061/9780872626874.035>.
- Marques, O. B., F. Feddersen, and J. MacMahan, 2024: An effective water depth correction for pressure-based wave statistics on rough bathymetry. *J. Atmos. Oceanic Technol.*, **41**, 1047–1062, <https://doi.org/10.1175/JTECH-D-23-0118.1>.
- , —, and —, 2025: Dataset for observations of wave energy dissipation by bottom friction on rocky shores. Zenodo, accessed 11 April 2025, <https://doi.org/10.5281/zenodo.15199472>.
- Mirfenderesk, H., and I. R. Young, 2003: Direct measurements of the bottom friction factor beneath surface gravity waves. *Appl. Ocean Res.*, **25**, 269–287, <https://doi.org/10.1016/j.apor.2004.02.002>.
- Monismith, S. G., 2007: Hydrodynamics of coral reefs. *Annu. Rev. Fluid Mech.*, **39**, 37–55, <https://doi.org/10.1146/annurev.fluid.38.050304.092125>.
- , J. S. Rogers, D. Kowek, and R. B. Dunbar, 2015: Frictional wave dissipation on a remarkably rough reef. *Geophys. Res. Lett.*, **42**, 4063–4071, <https://doi.org/10.1002/2015GL063804>.
- Moulton, M., S. H. Suanda, J. C. Garwood, N. Kumar, M. R. Fewings, and J. M. Pringle, 2023: Exchange of plankton, pollutants, and particles across the nearshore region. *Annu. Rev. Mar. Sci.*, **15**, 167–202, <https://doi.org/10.1146/annurev-marine-032122-115057>.
- Nelson, R. C., 1996: Hydraulic roughness of coral reef platforms. *Appl. Ocean Res.*, **18**, 265–274, [https://doi.org/10.1016/S0141-1187\(97\)00006-0](https://doi.org/10.1016/S0141-1187(97)00006-0).
- Nielsen, P., 1992: *Coastal Bottom Boundary Layers and Sediment Transport*. Vol. 4. World Scientific, 324 pp.
- Nunes, V., and G. Pawlak, 2008: Observations of bed roughness of a coral reef. *J. Coastal Res.*, **24**, 39–50, <https://doi.org/10.2112/05-0616.1>.
- OCM Partners, 2025: 2013 NOAA Coastal California Topobathy Merge Project. OCM Partners, accessed 19 May 2024, <https://www.fisheries.noaa.gov/inport/item/49649>.
- Péquignet, A.-C., J. M. Becker, M. A. Merrifield, and S. J. Boc, 2011: The dissipation of wind wave energy across a fringing reef at Ipan, Guam. *Coral Reefs*, **30**, 71–82, <https://doi.org/10.1007/s00338-011-0719-5>.
- Poate, T., G. Masselink, M. J. Austin, M. Dickson, and R. McCall, 2018: The role of bed roughness in wave transformation across sloping rock shore platforms. *J. Geophys. Res. Earth Surf.*, **123**, 97–123, <https://doi.org/10.1002/2017JF004277>.
- Raghukumar, K., G. Chang, F. Spada, C. Jones, T. Janssen, and A. Gans, 2019: Performance characteristics of “Spotter,” a newly developed real-time wave measurement buoy. *J. Atmos. Oceanic Technol.*, **36**, 1127–1141, <https://doi.org/10.1175/JTECH-D-18-0151.1>.
- Rogers, J. S., S. G. Monismith, D. A. Kowek, and R. B. Dunbar, 2016: Wave dynamics of a Pacific atoll with high frictional effects. *J. Geophys. Res. Oceans*, **121**, 350–367, <https://doi.org/10.1002/2015JC011170>.
- , S. A. Maticka, V. Chirayath, C. B. Woodson, J. J. Alonso, and S. G. Monismith, 2018: Connecting flow over complex terrain to hydrodynamic roughness on a coral reef. *J. Phys. Oceanogr.*, **48**, 1567–1587, <https://doi.org/10.1175/JPO-D-18-0013.1>.
- Rosman, J. H., and J. L. Hench, 2011: A framework for understanding drag parameterizations for coral reefs. *J. Geophys. Res.*, **116**, C08025, <https://doi.org/10.1029/2010JC006892>.
- Ruessink, B. G., J. R. Miles, F. Feddersen, R. T. Guza, and S. Elgar, 2001: Modeling the alongshore current on barred beaches. *J. Geophys. Res.*, **106**, 22 451–22 463, <https://doi.org/10.1029/2000JC000766>.
- Sallenger, A. H., Jr., and R. A. Holman, 1985: Wave energy saturation on a natural beach of variable slope. *J. Geophys. Res.*, **90**, 11 939–11 944, <https://doi.org/10.1029/JC090iC06p11939>.
- Sherwood, C. R., and Coauthors, 2022: Modeling the morphodynamics of coastal responses to extreme events: What shape are we in? *Annu. Rev. Mar. Sci.*, **14**, 457–492, <https://doi.org/10.1146/annurev-marine-032221-090215>.
- Simons, R. R., A. J. Grass, and A. Kyriacou, 1988: The influence of currents on wave attenuation. *Coastal Engineering 1988*, American Society of Civil Engineers, 363–376, <https://doi.org/10.1061/9780872626874.026>.
- Sleath, J. F. A., 1987: Turbulent oscillatory flow over rough beds. *J. Fluid Mech.*, **182**, 369–409, <https://doi.org/10.1017/S0022112087002374>.
- Smyth, C., and A. E. Hay, 2003: Near-bed turbulence and bottom friction during SandyDuck97. *J. Geophys. Res.*, **108**, 3197, <https://doi.org/10.1029/2001JC000952>.
- Sous, D., F. Bouchette, E. Doerflinger, S. Meule, R. Certain, G. Toulemonde, B. Dubarbar, and B. Salvat, 2020: On the small-scale fractal geometrical structure of a living coral reef barrier. *Earth Surf. Processes Landforms*, **45**, 3042–3054, <https://doi.org/10.1002/esp.4950>.
- , K. Martins, M. Tissier, F. Bouchette, and S. Meule, 2023: Spectral wave dissipation over a roughness-varying barrier reef. *Geophys. Res. Lett.*, **50**, e2022GL102104, <https://doi.org/10.1029/2022GL102104>.
- Swart, D. H., 1974: Offshore sediment transport and equilibrium beach profiles. Delft Hydraulics Laboratory Pub. 131, 323 pp., https://repository.tudelft.nl/file/File_233d3d2b-1feb-4c3d-9daa-e7b27d3db158.
- Thomson, J., J. B. Girton, R. Jha, and A. Trapani, 2018: Measurements of directional wave spectra and wind stress from a wave glider autonomous surface vehicle. *J. Atmos. Oceanic Technol.*, **35**, 347–363, <https://doi.org/10.1175/JTECH-D-17-0091.1>.
- Thornton, E. B., and R. T. Guza, 1982: Energy saturation and phase speeds measured on a natural beach. *J. Geophys. Res.*, **87**, 9499–9508, <https://doi.org/10.1029/JC087iC12p09499>.
- , and —, 1983: Transformation of wave height distribution. *J. Geophys. Res.*, **88**, 5925–5938, <https://doi.org/10.1029/JC088iC10p05925>.
- , and J. MacMahan, 2024: Update to friction factor formulations that impact rocky shores and coral reefs. *J. Geophys. Res. Oceans*, **129**, e2024JC021630, <https://doi.org/10.1029/2024JC021630>.
- Yu, X., J. H. Rosman, and J. L. Hench, 2018: Interaction of waves with idealized high-relief bottom roughness. *J. Geophys. Res. Oceans*, **123**, 3038–3059, <https://doi.org/10.1029/2017JC013515>.